Review of the KNMI clutter removal scheme

Iwan Holleman and Hans Beekhuis

Technical Report, KNMI TR-284, 2005

Contents

Chapter 1

Introduction

In the early 90s, a stepwise procedure for the rejection of (anomalous propagation) clutter has been developed and implemented in the C-band weather radars of KNMI (Wessels and Beekhuis, 1992, 1994). This procedure is based on distinguishing between the inherently fluctuating Rayleigh-scattered precipitation signals and the relatively stable ground clutter signals (Aoyagi, 1983). A dynamical clutter map is constructed from the "fluctuation" flags using a spatial averaging procedure and a decision-making model. Anomalous propagation clutter over land is removed almost completely, while the system is partly (40%) effective in removing sea clutter. All in all, the radar operators and customers are quite satisfied with the performance of this statistical clutter rejection method.

Nowadays most operational weather radars use Doppler filtering of the received power to suppress clutter from fixed targets. The spectral power around zero, i.e., from fixed targets, is cut from the Doppler spectrum. Modern signal processors reconstruct the Doppler spectrum using interpolation before the spectral moments are estimated (Siggia and Passarelli Jr., 2004). Clutter suppression using Doppler filtering is not without problems especially for S-band radars where the precipitation echoes are about 10 dB weaker than for C-band radars (Kessinger et al., 2004). The first dual-polarization Doppler radars are slowly being integrated in the operational networks and they offer additional possibilities to separate precipitation and clutter signals (Parent du Châtelet et al., 2004). Steiner and Smith (2002) have proposed the use of three-dimensional reflectivity structure for the automated detection of clutter. In particular the vertical extent of the radar echoes, their spatial variability, and vertical gradient of the intensity are fed into a decision tree. Sugier et al. (2002) have recently developed and implemented a statistical clutter removal scheme based on echo fluctuations. They report a high detection probability of fixed ground targets (96-99%) and a false alarm rate below 2%.

Currently KNMI is preparing a technical upgrade of the weather radar systems which are now running for almost 10 years. The purpose of the upgrade is to

ensure that the weather radars can operate for another 10 years. Apart from a mechanical overhaul the upgrade will consist of a renewal of the radar (scan) controller, the signal processor, and the product generator. The radar controller and the signal processor are 10-year-old computer systems which have become outdated and difficult to maintain. The technical upgrade is also the reason for the review of the current operational clutter removal scheme. For this review it is important to note that the demand for 3-dimensional volume data for research and operations is increasing.

In this technical report it is demonstrated that the current clutter removal scheme can be transformed to a method for 3-dimensional polar data by a few (minor) modifications. The performance of the proposed clutter rejection scheme has been evaluated using three cases. Furthermore a quantitative evaluation of the current and proposed clutter removal scheme using one month of radar data is presented. It is found that the proposed scheme produces cleaner reflectivity images where the residual clutter close to the radar and especially the sea clutter are removed more effectively. Therefore it is highly recommended to implement the proposed clutter rejection scheme during the technical upgrade of the KNMI weather radars. The outline of the remaining of the report is as follows:

- In chapter 2 a detailed description of the current operational clutter removal scheme based on several reports and specification documents is presented.
- The current clutter removal scheme can be transformed to a method for 3-dimensional polar data by a few minor modifications. In chapter 3 the prosed clutter rejection scheme is documented in detail and a case of mixed precipitation and clutter is used to illustrate the procedure.
- In chapter 4 an evaluation of the proposed clutter rejection scheme based on three cases, a case with mixed precipitation and clutter, a case where the radome is wet, and a case of severe anomalous propagation, is described. Furthermore a quantitative evaluation of the current and proposed clutter removal scheme using one month of (hourly) radar data is presented.
- In the last chapter the conclusions and recommendations for further application are made.

Chapter 2

Current operational clutter removal scheme

In the early 90s, a stepwise procedure for rejection of (anomalous propagation) ground clutter has been developed and implemented at KNMI (Wessels and Beekhuis, 1992, 1994; Wessels, 2003). This procedure is based on distinguishing between the inherently fluctuating Rayleigh-scattered precipitation signals and the relatively stable ground clutter signals (Aoyagi, 1983). The first and the second step are performed by the radar preprocessor (Sigmet, 1998; Gematronik, 1996a), and the final step is evaluated by the processing software (Gematronik, 2003, 1996b).

Currently, the ground clutter rejection system has been operational for about 10 years. The system requires hardly any maintenance and can be applied up to long ranges (320 km). Anomalous propagation clutter over land is removed almost completely, while the system is partly (40%) effective in removing sea clutter. All in all, the radar operators and customers of the data are quite satisfied with its performance.

2.1 Clutter signal processing

The clutter signal processing is based on the raw Analog-to-Digital (AD) counts of the logarithmic channel of the receiver without (range) correction. The resolution of the AD samples of the current signal processor (Sigmet, 1998) is approximately 0.5 dBm for echoes well above the background noise and the sample frequency of the AD converter is 1.2 MHz. In figure 2.1 a schematic overview of the available range samples in processed range bin of 1 km $\times$ 1 degree is presented. The size of processed range bin is marked by the bold square and the raw range samples are indicated by the small boxes. Given the sample frequency of the AD converter,

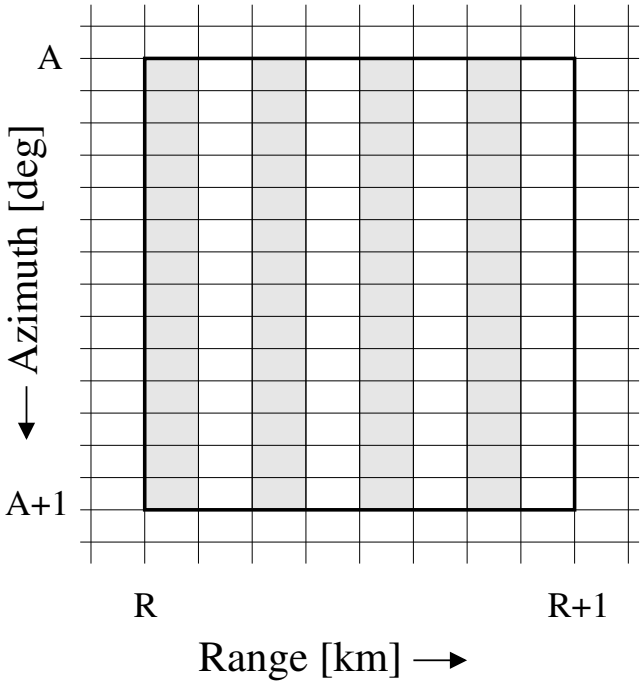

Figure 2.1: Schematic view of the AD samples in azimuthal and range direction of the received power in units of dBm that are the input for the clutter signal processing. The radar signal processor can obtain 8 samples per km and 14 samples per degree given a PRF of 250 Hz and an antenna rotation of 3 rpm. Only 4 samples per km are currently used in the clutter signal processing. The bold square in the figure indicates the size of a processed range bin which is 1 km $\times$ 1 degree.

maximum 8 samples per 1 km range are available for the (clutter) signal processing. Wessels and Beekhuis (1994) have shown that the range samples are (almost) uncorrelated when 4 samples per km are considered. With a Pulse Repetition Frequency (PRF) of 250 Hz and an azimuth speed of 18 degrees/s (3 rpm), about 14 samples are taken per 1 degree in azimuthal direction. Because of the finite beam width of the radar antenna (1 degree), the samples in azimuthal direction will be smoothed and thus will be correlated to a certain extent. So for each range bin maximum 112 samples of the received logarithmic power can be used for the clutter signal processing.

During the clutter signal processing the fluctuations of the received power (echoes) within each processed range bin are analyzed. This analysis requires a good synchronization of the AD sampling to the pulse transmission time, typically within 10 ns, and the power stability of the transmitted pulses should be around 0.2 dB or better. Furthermore, correction for the actual gain curve of the logarithmic receiver is of crucial importance for an accurate estimation of the intensity

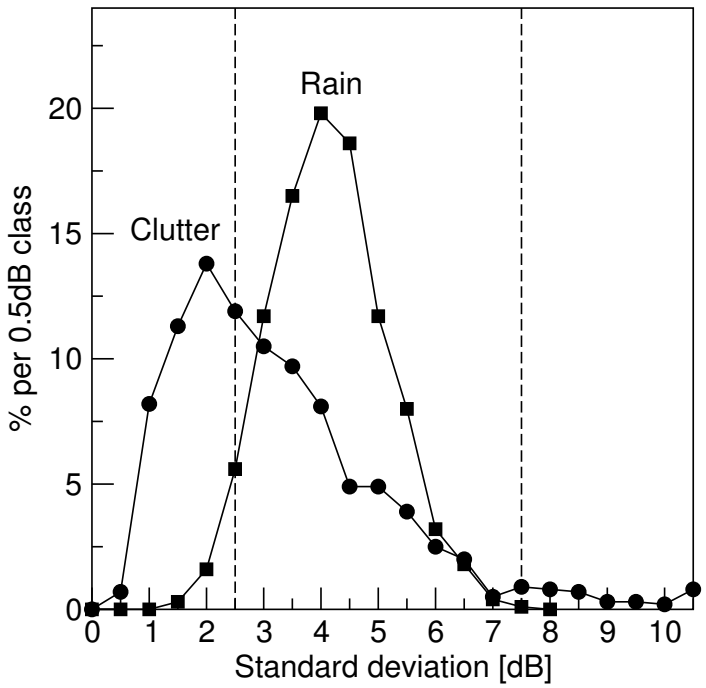

Figure 2.2: Examples of standard deviation spectra for precipitation and anomalous propagation clutter. The vertical dashed lines mark the thresholds that are used to make the distinction between precipitation and clutter in the first step of the algorithm (Figure taken from Wessels and Beekhuis (1994)).

fluctuations. The first step in the clutter signal processing is the calculation of a 5-point running average P_5 of the raw samples of the received power $P(r, a)$ in azimuthal direction (Wessels and Beekhuis, 1992):

$$P_5(r, a) \equiv \frac{1}{5} \sum_{\alpha=a-2}^{a+2} P(r, \alpha) \tag{2.1}$$

where r and a are the indices of the raw samples in range and azimuthal direction, respectively. Using the 5-point running average, the standard deviation of the raw power samples σ_p within the processed range bin is calculated:

$$\sigma_p(r, A) \equiv \sqrt{\frac{1}{N_a} \sum_{\alpha=0}^{N_a-1} [P(r, \alpha) - P_5(r, \alpha)]^2} \tag{2.2}$$

where A indicates the azimuth of the processed range bin and N_a is the number of azimuthal samples within a processed range bin ($N_a = 14$). In figure 2.2 examples of the standard deviation spectra of the raw power samples for areas with

precipitation and clutter are shown. The precipitation spectrum peaks around a standard deviation of 4.2 dB and the clutter spectrum peaks around 2.0 dB. The echoes from precipitation areas are caused by Rayleigh scattering and for this scattering process from random targets a standard deviation of 5.5 dB is expected from theory. The observed standard deviation is somewhat lower which is probably caused by the (small) correlation of the samples in azimuthal direction. The vertical dashed lines mark the thresholds that are used to make the distinction between precipitation and clutter signals. Evidently there is a large overlap between the standard deviation spectra for precipitation and clutter, and thus the separation of precipitation and clutter signals based on this criterion will not be good enough: about 45% of the clutter signals will be detected (Wessels and Beekhuis, 1994). Information from neighboring samples is, therefore, needed to improve the performance.

The standard deviation thresholds used to discriminate between precipitation and clutter are indicated by the dashed lines in figure 2.2. Actually the standard deviation thresholds, $\sigma_{min} \simeq 2.5$ dB and $\sigma_{max} \simeq 7.5$ dB, depend on the average power (Wessels and Beekhuis, 1992). The average power is calculated from the raw samples as follows:

$$\bar{P}(r, A) = \frac{1}{N_a} \sum_{\alpha=0}^{N_a-1} P(r, \alpha) \tag{2.3}$$

and this value is used to select appropriate values from the tabulated standard deviation thresholds. The use of these tabulated thresholds allows for a correction of the "non-log" behavior of the logarithmic receiver. In operational practice the logarithmic receiver has to be checked regularly and —if necessary— the tabulated thresholds have to be updated. The clutter flag for a certain range sample $c(r, A)$ is set according to:

$$c(r, A) = \begin{cases} 0 & \text{if} \quad \sigma_{min} \leq \sigma_p(r, A) \leq \sigma_{max} \\ 1 & \text{else} \end{cases} \tag{2.4}$$

where 1 indicates that there may be clutter in this range sample. For each processed range bin 8 of these flags could be obtained, but in order to be compliant with the old radar signal processor and to ensure statistical independence of the flags only 4 values, i.e., every 250 m, are currently used in further processing. The clutter flag for the processed range bin of 1 km $\times$ 1 degree $C(R, A)$ is set according to:

$$C(R, A) = \begin{cases} 0 & \text{if} \quad \sum_{\rho=0}^{3} c(r + 2\rho, A) < 2 \\ 1 & \text{else} \end{cases} \tag{2.5}$$

Table 2.1: Default values of the parameters for the current clutter flag processing. The dimensions of the areas are given in number of processed range bins (1 km $\times$ 1 deg).

Parameter	Value	Parameter	Value
ΔA_{in}	3	ΔR_{in}	6
ΔA_{out}	9	ΔR_{out}	18
ΔA_{std}	5	ΔR_{std}	10
dBZ_t	1 dBZ		

where R indicates the range of the processed range bin. These clutter flags and the corresponding reflectivity data are transferred as polar volume files to the radar product generator for further processing.

2.2 Clutter flag processing

The quality of the clutter flags $C(R, A)$ obtained from the processed range bins with a size of 1 km $\times$ 1 degree is still not good enough: about 61% of the clutter will be detected (Wessels and Beekhuis, 1994). A further processing of the clutter flags is needed before they can be applied to enhance the reflectivity data. The quality of clutter flags is increased by a spatial averaging procedure of the flags combined with a decision-making model. The first step in the spatial averaging procedure is a pairwise combination of the processed range bins into "twin bins" with a size of 2 km $\times$ 1 degree. The twin bins are approaching the size of the polar stereographic grid that KNMI uses for display of its radar products (2.4×2.4 km^2). In figure 2.3 a schematic view of the spatial averaging procedure of the twin bins is presented. The spatial extent of the averaging is determined by size of inner ($\Delta A_{in} \times \Delta R_{in}$) and outer ($\Delta A_{out} \times \Delta R_{out}$) squares in the figure. The default values are listed in table 2.1. Because most precipitation systems and clutter areas are larger than 10 km $\times$ 5 degrees, this spatial averaging has only a minor effect on the spatial resolution. In this way, about 98% of the clutter will be detected while less than 1% of rain pixels will be removed (Wessels and Beekhuis, 1994).

The spatial averaging procedure is based on reflectivity flags N_{R2} and clutter flags T_{R2} for the twin bins. Both reflectivity values within a twin bin are compared to a threshold value dBZ_t (default 1 dBZ), giving two reflectivity subflags which are added in the flag $N_{R2} = 0, 1, 2$. The two clutter subflags $C(R, A)$, which are only considered when the corresponding reflectivity subflag is set, are added in flag $T_{R2} = 0, 1, 2$. Note that the value of the clutter flag can never be

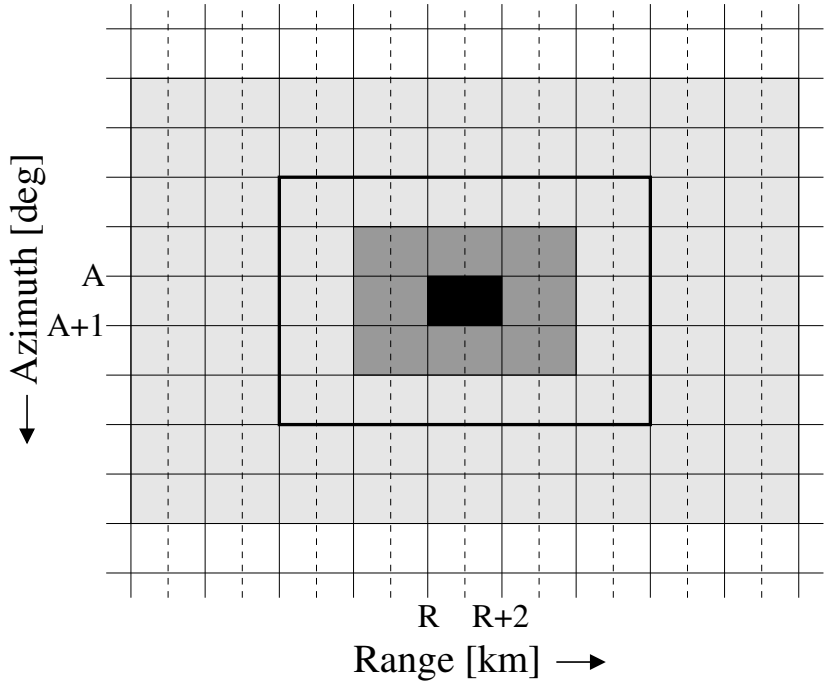

Figure 2.3: Schematic view of the spatial averaging procedure of the reflectivity and clutter flags is presented. The small rectangular boxes represent the so-called "twin bins" that are a pairwise combination of processed range bins (indicated by the dashed lines). The central twin bin is marked in black, and the inner and outer areas are colored with dark gray and light gray, respectively. The bold square indicates the area where the horizontal fluctuations of the reflectivity pattern is analyzed.

higher than that of the corresponding reflectivity flag. If reflectivity data for obstructed azimuths have been replaced by data from nearby azimuths ("Occultation correction"), the clutter flags are replaced as well.

Before the further spatial averaging is performed, the reflectivity and clutter flags of the twin bins at different elevations (default 4 elevations: 0.3, 1.1, 2.0, 3.0 degrees) are combined into a low altitude pseudoCAPPI image. The clutter and reflectivity flags are taken from the elevation with the highest weight in the pseudoCAPPI image. When the radome is wetted by rain, nearby ground returns increase because of increased antenna sidelobes. Even observations at 3.0 deg. elevation, used for short-ranges in the pseudoCAPPIs image, show ground echoes that are added to the echoes from nearby rain. The resulting echo is more stable than precipitation and therefore may be classified as clutter. Therefore clutter flags up to a certain range (25 km) are ignored for those azimuths where the echo at a predefined range (15 km) exceeds a predefined value (6 dBZ).

The procedure for the spatial averaging of the reflectivity and clutter flags is illustrated in figure 2.3. Around each twin bin an outer area measuring $\Delta R_{out} \times \Delta A_{out}$ and an inner area measuring $\Delta R_{in} \times \Delta A_{in}$ are defined. The central twin bin is part of both the outer and the inner areas. In the following this twin bin receives additional weight in the decision-making model, and thus the smoothing weight factors approximate a Bell-shape around the central twin bin. The sum of the reflectivity flags N is made over the inner and outer areas around each twin bin:

$$N = \sum_{\rho=-\delta R_o}^{\delta R_o} \sum_{\alpha=-\delta A_o}^{\delta A_o} N_{R2}(\rho,\alpha) + \sum_{\rho=-\delta R_i}^{\delta R_i} \sum_{\alpha=-\delta A_i}^{\delta A_i} N_{R2}(\rho,\alpha). \tag{2.6}$$

The summation limits $\delta R_{i,o}$ and $\delta A_{i,o}$ in the preceding equation are defined by:

$$\delta A_{i,o,s} = (\Delta A_{in,out,std} - 1)/2 \tag{2.7}$$

$$\delta R_{i,o,s} = (\Delta R_{in,out,std} - 2)/4 \tag{2.8}$$

where an additional factor of two has been introduced in the equations for δR to account for the size of the "twin bins". Similarly the sum of the clutter flags T is made over the inner and outer areas around each twin bin:

$$T = \sum_{\rho=-\delta R_o}^{\delta R_o} \sum_{\alpha=-\delta A_o}^{\delta A_o} T_{R2}(\rho,\alpha) + \sum_{\rho=-\delta R_i}^{\delta R_i} \sum_{\alpha=-\delta A_i}^{\delta A_i} T_{R2}(\rho,\alpha). \tag{2.9}$$

In the above summations for N and T, a periodic boundary condition in the summations over α is applied and the last value of ρ is assumed to be valid beyond the natural limits (zero and maximum range). The maximum possible value of N and T is given by:

$$N_s = \Delta R_{in}\Delta A_{in} + \Delta R_{out}\Delta A_{out} \tag{2.10}$$

where N_s is used for normalizing the summations of the reflectivity and clutter flags.

Apart from the summed reflectivity and clutter flags, the standard deviation of the observed reflectivity over a pre-defined area around the central twin bin (bold square in figure 2.3) is calculated. This standard deviation is corrected for the local reflectivity gradients in tangential and radial direction by two-dimensional least squares fitting. For this fitting the following intermediate quantities are calculated:

$$S = \Delta R_{std}\Delta A_{std} \tag{2.11}$$

$$S_z = \sum_{\rho=-\delta R_s}^{\delta R_s} \sum_{\alpha=-\delta A_s}^{\delta A_s} Z_{R2}(\rho,\alpha) \tag{2.12}$$

$$S_{zr} = \sum_{\rho=-\delta R_s}^{\delta R_s} \sum_{\alpha=-\delta A_s}^{\delta A_s} \rho Z_{R2}(\rho,\alpha) \tag{2.13}$$

$$S_{za} = \sum_{\rho=-\delta R_s}^{\delta R_s} \sum_{\alpha=-\delta A_s}^{\delta A_s} \alpha Z_{R2}(\rho,\alpha) \tag{2.14}$$

$$S_{rr} = \sum_{\rho=-\delta R_s}^{\delta R_s} \sum_{\alpha=-\delta A_s}^{\delta A_s} \rho^2 \tag{2.15}$$

$$S_{aa} = \sum_{\rho=-\delta R_s}^{\delta R_s} \sum_{\alpha=-\delta A_s}^{\delta A_s} \alpha^2 \tag{2.16}$$

where the twin bin reflectivity $Z_{R2}(R,A)$ is the average over the underlying range bins and the summation limits are obtained from equation 2.7. Note that because of symmetry the quantities S_r, S_a, and S_{ra} are zero. From the intermediate quantities the average reflectivity c and the reflectivity gradients in radial a and tangential b direction can be calculated:

$$a = \frac{S_{zr}}{S_{rr}} \tag{2.17}$$

$$b = \frac{S_{za}}{S_{aa}} \tag{2.18}$$

$$c = \frac{S_z}{S}. \tag{2.19}$$

Using the results from the least squares fitting, the standard deviation of the corrected reflectivity is calculated using:

$$\sigma_Z = \sqrt{\frac{S_{zz}^{(2)}}{S} - \left(\frac{S_z^{(2)}}{S}\right)^2} \tag{2.20}$$

where $S_z^{(2)}$ and $S_{zz}^{(2)}$ are defined as:

$$S_z^{(2)} = \sum_{\rho=-\delta R_s}^{\delta R_s} \sum_{\alpha=-\delta A_s}^{\delta A_s} (Z_{R2}(\rho,\alpha) - a\rho - b\alpha - c) \tag{2.21}$$

$$S_{zz}^{(2)} = \sum_{\rho=-\delta R_s}^{\delta R_s} \sum_{\alpha=-\delta A_s}^{\delta A_s} (Z_{R2}(\rho,\alpha) - a\rho - b\alpha - c)^2 \tag{2.22}$$

The clutter decision-making model is based on the local values of T_{R2}, N, σ_Z and T.

The threshold curves for making the final decision whether a twin bin is contaminated by clutter or not are displayed in figure 2.4. The upper frame shows the threshold curves for short ranges and the lower frame shows them for long ranges. A smooth transition between the two regimes is made. When the clutter fraction

a)

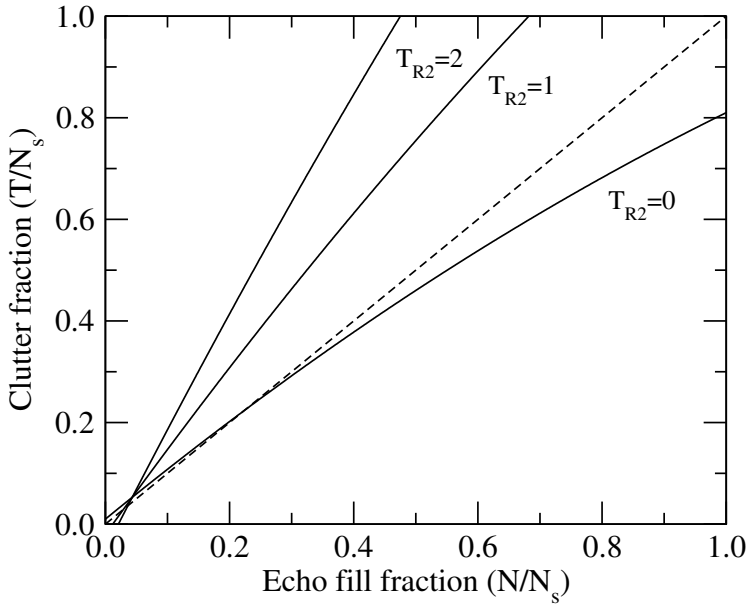

b)

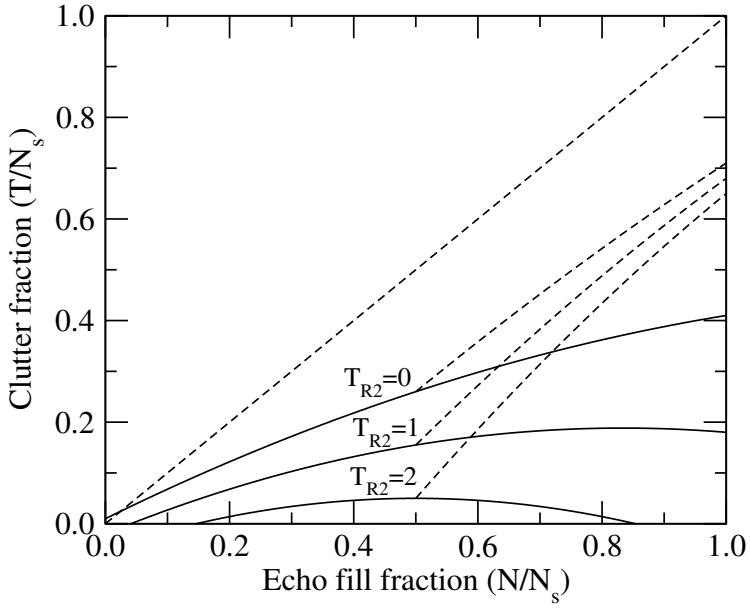

Figure 2.4: The threshold curves of the clutter decision making model are displayed in this figure. The upper frame **a)** shows the threshold curves for short ranges from the radar, and the lower frame **b)** shows them for long ranges. Three different threshold curves, one for each possible value of the clutter flag of the central twin bin T_{R2}, are presented in both frames.

Table 2.2: Default values of the constants for the current clutter decision-making model as developed by Wessels and Beekhuis (1994).

Constant	Value	Constant	Value
C_{00}	0.60	C_{rt}	0.40
C_{01}	-0.10	C_{d0}	1.00
C_{20}	-0.20	C_{d1}	2.00
C_{21}	-0.10		
C_{30}	0.01	$C_h(0)$	-0.30
C_{31}	-0.03	$C_h(1)$	-0.50
C_{r0} [km]	1.40	$C_h(2)$	-0.70
η_t	0.5	σ_t	3.5 dBZ

T/N_s (on y-axis) for a certain echo-fill fraction N/N_s (on x-axis) is higher than the threshold curve, the final clutter flag for the corresponding twin bin is set. Three different threshold curves, one for each possible value of the clutter flag of the central twin bin T_{R2}, are presented in figure. The diagonal dashed line ($y = x$) indicates the maximum value of T for a given N, because T cannot be larger than N.

The rationale behind these threshold curves for long ranges (Wessels and Beekhuis, 1994) is that twin bins with both clutter subflags set ($T_{R2} = 2$) are almost automatically classified as cluttered, independent of the properties of the surrounding twin bins. On the other hand, twin bins with $T_{R2} = 0$ can also acquire a final clutter flag, especially when they are embedded in a massive echo ($N/N_s \simeq 1$) with at least 40% clutter flags according to T/N_s. An important condition is that isolated echoes ($N = 1$ or 2) without any clutter subflags ($T_{R2} = 0$) should not be considered as clutter in order to avoid removal of the first signature of a developing storm. This can be achieved by making sure that corresponding threshold is positive for $N/N_s \simeq 0$. During the first few years of operation, areas with stratiform rain (mostly from warm fronts) were falsely classified as clutter and thus burning a “hole” in the precipitation pattern. To fix this problem, the horizontal fluctuations of the reflectivity pattern are analyzed using the gradient-corrected standard deviation (Wessels, 2003) and for areas with small fluctuations the clutter thresholds are raised (dashed curves in figure 2.4).

At short ranges, (weak) clutter from to the sidelobes of the antenna is usually seen. In the case of nearby rain, a combined clutter and precipitation signal is received and the resulting echo is more stable than precipitation alone. Using the long-range threshold curves, this echo would be flagged as clutter and thus a hole (reflecting the sidelobe pattern) would be created in the observed precipitation at

short ranges. Therefore the threshold curves for short ranges are raised to fall above (near) the $y = x$ line, so that the clutter flags will not (hardly ever) be set.

The threshold curves of the clutter decision-making model shown in figure 2.4 are described by second-order polynomials (Wessels and Beekhuis, 1994). The constants of the polynomials are constructed using the following equations:

$$C_0 = C_{00} + C_{01}T_{R2} \tag{2.23}$$

$$C_d = \min(C_{rt}, C_{r0}/R) \cdot (C_{d0} + C_{d1}T_{R2}) \tag{2.24}$$

$$C_2 = C_{20} + C_{21}T_{R2} \tag{2.25}$$

$$C_3 = C_{30} + C_{31}T_{R2} \tag{2.26}$$

$$C_4 = \begin{cases} -\frac{N/N_s - \eta_t}{1-\eta_t} \cdot C_h(T_{R2}) & \text{if} \quad N/N_s > \eta_t \wedge \sigma_Z < \sigma_t \\ 0 & \text{else} \end{cases} \tag{2.27}$$

where the central twin bin is at range R in km, η_t is the threshold on the echo fill fraction, and σ_t is the threshold on the reflectivity standard deviation. The values of the constants are listed in table 2.2. Using these five constants the threshold polynomial is given by:

$$\left(\frac{T_t}{N_s}\right) \equiv C_4 + C_3 + (C_0 + C_d) \cdot \left(\frac{N}{N_s}\right) + C_2 \cdot \left(\frac{N}{N_s}\right)^2 \tag{2.28}$$

where T_t is the threshold value for the summed clutter flags T around the central twin bin. If T is larger than T_t and the corresponding reflectivity flag is set, the final clutter flag for the central twin bin is also set.

Finally, the polar pseudoCAPPI reflectivity image and clutter map are transfered to a Cartesian grid and subsequently to a rectangular picture in polar stereographic projection (KNMI standard). This coordinate conversion is done by resampling the value of the nearest pixel of the originating grid and the clutter flags accompany the reflectivity values during the conversion process.

2.3 Clutter flag application

The Cartesian reflectivity images and corresponding clutter maps are transferred to the radar compositing and distribution system (so-called VCRIS), where the clutter map is overlayed on the reflectivity image. Subsequently, the cleaned reflectivity images from both radars are combined into the KNMI radar composite. Because the actual clutter removal is carried out in the compositing and distribution system, it remains possible to distribute radar products with clutter as well as cleaned products. In figure 2.5 a flow diagram for the current implementation of the clutter rejection algorithm is presented. The application of the clutter algorithm is distributed over the signal processor (Sigmet, 1998), the product generator (Gematronik, 2003), and the compositing and distribution system (VCRIS).

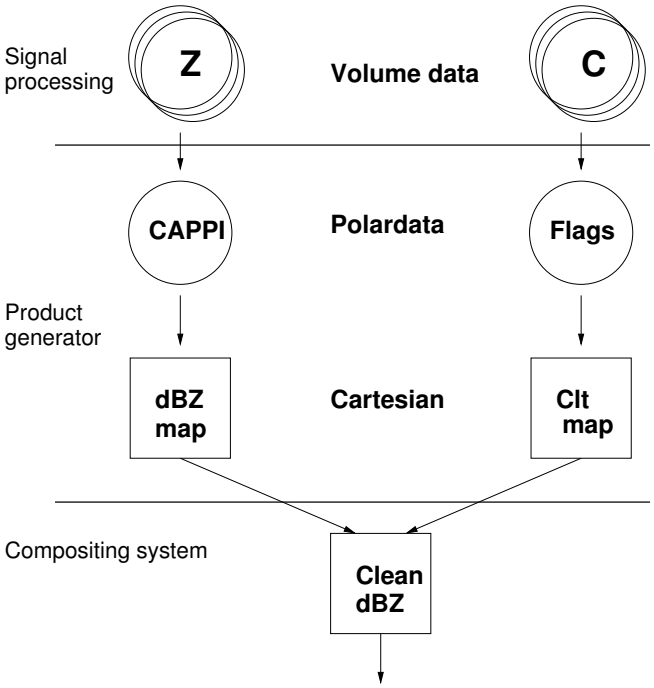

Figure 2.5: Flow diagram for the current implementation of the clutter rejection algorithm. On the left the systems where action is taken, i.e., the signal processor, the product generator, and the compositing system, are indicated

Chapter 3

Proposed update of clutter removal scheme

Currently KNMI is preparing a technical upgrade of the weather radar systems which are now running for almost 10 years. The purpose of the upgrade is to ensure that the weather radars can operate for another 10 years. Apart from a mechanical overhaul the upgrade will consist of a renewal of the radar (scan) controller, the signal processor, and the product generator. The radar controller and the signal processor are 10-year-old computer systems which have become outdated and difficult to maintain. The technical upgrade is also the reason for the review of the current operational clutter removal scheme which is running for more than 10 years and performing rather well. For this review it is important to note that the radar products with clutter are not distributed anymore and that the demand for the 3-dimensional volume data for research and operations is increasing. Therefore the review of the clutter removal scheme is focused on a transformation from a method for 2-dimensional Cartesian images to a method for 3-dimensional polar data.

It will be shown in this chapter that the current clutter removal scheme can be transformed to a method for 3-dimensional polar data by a few (minor) modifications. This transformation of the clutter removal scheme has the following advantages, it:

- enables the production of 3-dimensional volume data without clutter that can be considered the base data from the weather radar systems in the (near) future.

- can be implemented completely in the radar signal processor and thus simplifying the radar processing chain. Currently the implementation of the clutter removal scheme is distributed over three systems (see figure 2.5).

- becomes feasible to apply different clutter rejection or filtering methods for different elevations in a scanned volume. Application of e.g. Doppler clutter filtering at higher elevations allows for faster scanning and combination of Doppler and reflectivity scans.

- will provide polar reflectivity data at 1 km range resolution instead of 2 km. An increase of the horizontal resolution of the KNMI reflectivity composite and derived hydrological products can then be considered.

- probably improves the performance of the clutter removal because conceptual problems with the pseudoCAPPI weighting of clutter flags, i.e., "How to weight a flag?", are circumvented.

- improves the performance because accuracy problems with the separate projection to a Cartesian image of the reflectivity data and the corresponding clutter flags are circumvented.

In the following sections the modifications of the clutter removal scheme will be described for the three processes highlighted in previous chapter, i.e., clutter signal processing, clutter flag processing, and clutter flag application.

3.1 Clutter signal processing

The new clutter signal processing will basically be identical to the old clutter signal processing described in section 2.1. A few simplifications are possible because the analog (logarithmic) receiver will be replaced by a digital IF (Intermediate Frequency) receiver. The digital IF signal processor employs samples of the linear In-phase (I) and Quadrature phase (Q) channels for the processing, and the received power in dBm is calculated from the linear channels. For a digital receiver, the correction for the "non-log" behavior of the logarithmic receiver based on the tabulated standard deviation thresholds is not needed anymore and fixed thresholds will do.

The samples of the received power in dBm (or the reflectivity in dBZ) calculated from the linear I and Q channels and corrected for the background noise are the input for the new clutter signal processing (see figure 2.1). From these raw power samples the 5-point running average P_5 is calculated in azimuthal direction using equation 2.1. The standard deviation of the power samples σ_p is calculated from the actual values and the 5-point running average using equation 2.2. With a PRF of 250 Hz and an azimuth speed of 18 degrees/s, about 14 independent raw power samples per 1 degree are available for calculation of the standard deviation.

Table 3.1: Default values of the parameters for the new clutter signal processing. By default the number of samples per processed range bins and clutter threshold are 4 and 2 respectively.

Parameter	Value [Unit]
PRF	250 Hz
Azimuthal speed	18 deg/s
Range bin size	1 km $\times$ 1 deg
Samples per bin	4 or 8
Clutter threshold	2 or 3/4
Minimum std. dev.	2.5 dB
Maximum std. dev.	7.5 dB

Using fixed minimum threshold σ_{min} and maximum threshold σ_{max}, i.e., not depending on the received power, the clutter flag for a certain range sample is set depending on the observed standard deviation (see equation 2.4).

The clutter flag for the processed range bin is based on the flags for the underlying range samples. Up to 8 samples per processed range bin can be obtained, but the current clutter signal processing is based on 4 flags per processed range bin to ensure statistical independence. Equation 2.5 is used to set the clutter flag $C(R, A)$ for the processed range bin when 4 samples per range bin are used. When 8 samples per range bin are used, the clutter flag $C(R, A)$ is set according to:

$$C(R,A) = \begin{cases} 0 & \text{if} \quad \sum_{\rho=0}^{7} c(r+\rho, A) < C_t \\ 1 & \text{else} \end{cases} \tag{3.1}$$

where the optimum threshold C_t either 3 or 4 has to be determined. This optimum threshold is non-trivial because the statistical correlation of the 125 m samples is most likely stronger than that of the 250 m samples. Note that the length of the radar pulse volume is 300 m for 2 μs transmission pulses. The current signal processor cannot process 8 samples per km to 320 km range, but the new digital IF signal processor will probably be capable of doing so.

3.2 Clutter flag processing

Most modifications of the clutter removal scheme are made in the clutter flag processing. Because the range resolution of the 3-dimensional volume data has to be retained, the construction of the so-called twin bins (see figure 2.3) in the current

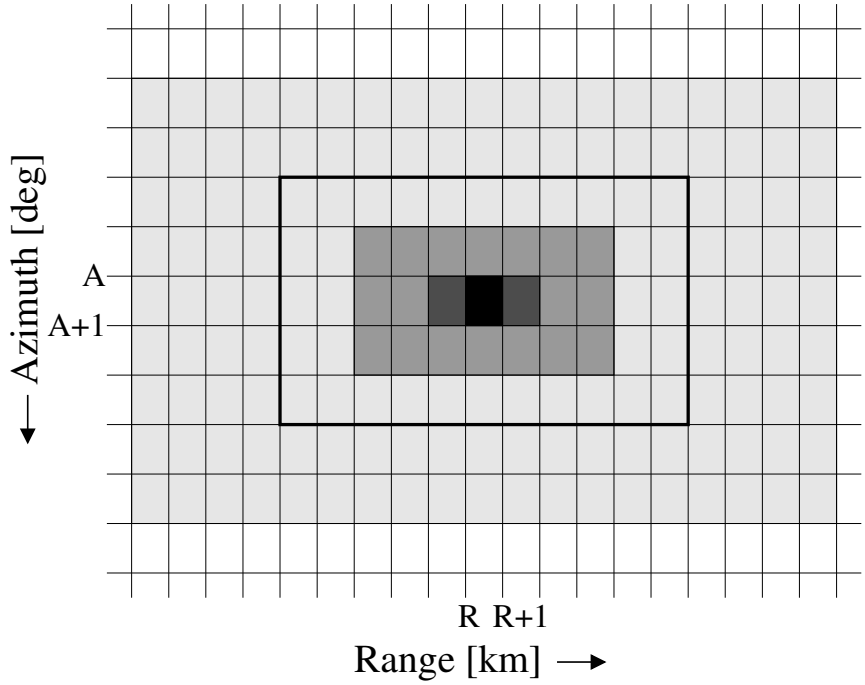

Figure 3.1: Schematic view of the proposed spatial averaging procedure of the reflectivity and clutter is presented. The central range bin and the two neighbors are marked in black and almost black, respectively, and the inner and outer areas are colored with dark gray and light gray, respectively. The bold square indicates the area where the horizontal fluctuations of the reflectivity pattern is analyzed.

clutter flag processing has to be abandoned. The wet radome correction is abandoned because its functionality largely overlaps with that of the range-dependent decision-making model. In addition the occultation correction, i.e., replacement of data for obstructed azimuths by interpolated data from neighboring azimuths, will be implemented as a separate process after the clutter rejection. This simplifies the processing chain considerably and will only have a minor impact on the data quality. Furthermore the combination of the reflectivity and clutter flags at different elevations into a low altitude pseudoCAPPI image is dropped. Finally the second-order polynomials that describe the threshold curves of the clutter decision-making model (see figure 2.4) are reformulated to simplify their construction and to make the model more flexible.

In figure 3.1 a schematic view of the proposed spatial averaging procedure of the reflectivity and clutter flags is presented. The reflectivity flags for the processed range bins N_R are set when the observed reflectivity exceeds a certain threshold value dBZ_t (default 1 dBZ). The clutter flags T_R are copied from equation 2.5 or 3.1 but are only considered when the corresponding reflectivity flag is

Table 3.2: Default values of parameters for the proposed clutter flag processing. The dimensions of the areas are given in number of processed range bins (1 km $\times$ 1 deg).

Parameter	Value	Parameter	Value
ΔA_{in}	3	ΔR_{in}	7
ΔA_{out}	9	ΔR_{out}	19
ΔA_{std}	5	ΔR_{std}	11
dBZ_t	1 dBZ	η_t	0.5
σ_t	3.5 dBZ		

set. The central range bin and its two neighbors are marked in black and almost black, respectively, in the figure, and the inner and outer areas are colored with dark gray and light gray, respectively. The outer area is measuring $\Delta R_{out} \times \Delta A_{out}$ and the inner area is measuring $\Delta R_{in} \times \Delta A_{in}$. The default values are listed in table 3.2. Similarly to the spatial averaging procedure for twin bins, the reflectivity and clutter flags for the range bins are summed into N and T, approximating a Bell-shape. The sum of the reflectivity flags N is made over the inner and outer areas around each processed range bin:

$$N = \sum_{\rho=-\delta R_o}^{\delta R_o} \sum_{\alpha=-\delta A_o}^{\delta A_o} N_R(\rho,\alpha) + \sum_{\rho=-\delta R_i}^{\delta R_i} \sum_{\alpha=-\delta A_i}^{\delta A_i} N_R(\rho,\alpha) \tag{3.2}$$

where the summation limits $\delta R_{i,o}$ and $\delta A_{i,o}$ are defined by:

$$\delta A_{i,o,s} = (\Delta A_{in,out,std} - 1)/2 \tag{3.3}$$

$$\delta R_{i,o,s} = (\Delta R_{in,out,std} - 1)/2. \tag{3.4}$$

Note that the equation for δR differs by a factor of two from the previous equation because processed range bins are now accumulated instead of twin bins. In the same way the sum of the clutter flags T is made over the inner and outer areas around each processed range bin:

$$T = \sum_{\rho=-\delta R_o}^{\delta R_o} \sum_{\alpha=-\delta A_o}^{\delta A_o} T_R(\rho,\alpha) + \sum_{\rho=-\delta R_i}^{\delta R_i} \sum_{\alpha=-\delta A_i}^{\delta A_i} T_R(\rho,\alpha). \tag{3.5}$$

In the above summations for N and T, a periodic boundary condition in the summations over α is applied again and the last value of ρ is assumed to be valid beyond the natural limits (zero and maximum range). The maximum possible value of N and T is given by equation 2.10.

The standard deviation of the observed reflectivity over a pre-defined area around the range bin (bold square in figure 3.1) is calculated. This standard deviation is corrected for the local reflectivity gradients in tangential and radial direction by two-dimensional least squares fitting. Equations 2.11 and 2.21 have been rewritten so that the standard deviation σ_Z can be calculated in a single summation. For this fitting the following intermediate quantities are calculated:

$$S = \Delta R_{std} \Delta A_{std} \tag{3.6}$$

$$S_{rr} = \delta R_{std} \cdot (2\delta R_{std}^2 + 3\delta R_{std} + 1) \cdot \Delta A_{std}/3 \tag{3.7}$$

$$S_{aa} = \delta A_{std} \cdot (2\delta A_{std}^2 + 3\delta A_{std} + 1) \cdot \Delta R_{std}/3 \tag{3.8}$$

$$S_z = \sum_{\rho=-\delta R_s}^{\delta R_s} \sum_{\alpha=-\delta A_s}^{\delta A_s} Z_R(\rho, \alpha) \tag{3.9}$$

$$S_{zz} = \sum_{\rho=-\delta R_s}^{\delta R_s} \sum_{\alpha=-\delta A_s}^{\delta A_s} Z_R^2(\rho, \alpha) \tag{3.10}$$

$$S_{zr} = \sum_{\rho=-\delta R_s}^{\delta R_s} \sum_{\alpha=-\delta A_s}^{\delta A_s} \rho Z_R(\rho, \alpha) \tag{3.11}$$

$$S_{za} = \sum_{\rho=-\delta R_s}^{\delta R_s} \sum_{\alpha=-\delta A_s}^{\delta A_s} \alpha Z_R(\rho, \alpha) \tag{3.12}$$

where $Z_R(R, A)$ represents the observed reflectivity in a range bin and the summation limits are obtained from equation 3.3. The intermediate quantities S_r, S_a, and S_{ra} are zero because of symmetry. For the analytical evaluation of intermediate quantities S_{rr} and S_{aa} the following expression has been used:

$$\sum_{n=0}^{N} n^2 = \frac{1}{6} N(2N^2 + 3N + 1). \tag{3.13}$$

From the intermediate quantities the standard deviation of the gradient-corrected reflectivity is calculated using:

$$\sigma_Z = \sqrt{\frac{S_{zz}}{S} - \frac{S_{zr}^2}{S_{rr} S} - \frac{S_{za}^2}{S_{aa} S} - \frac{S_z^2}{S^2}}. \tag{3.14}$$

Based on this standard deviation and the summed reflectivity flags N the standard deviation flag S_R for the central range bin is set:

$$S_R = \begin{cases} 1 & \text{if} \quad N/N_s > \eta_t \wedge \sigma_Z < \sigma_t \\ 0 & \text{else} \end{cases} \tag{3.15}$$

where the threshold on the echo fill fraction is η_t and that on the reflectivity standard deviation is σ_t. Note that the standard deviation only has to be calculated

Table 3.3: Default values of the constants for the proposed clutter decision-making model as a function of the triple clutter flag T_{R3} and the standard deviation flag S_R. The default value for the minimum range R_0 is 7.0 km.

$S_R = 0$	$T_{R3} = 0$	$T_{R3} = 1$	$T_{R3} = 2$	$T_{R3} = 3$
A	-0.20	-0.30	-0.40	-0.50
B	0.60	0.50	0.40	0.30
B'	0.40	1.20	2.00	2.80
C	0.01	-0.02	-0.05	-0.08
$S_R = 1$	$T_{R3} = 0$	$T_{R3} = 1$	$T_{R3} = 2$	$T_{R3} = 3$
A	-0.20	-0.30	-0.40	-0.50
B	1.20	1.50	1.80	2.10
B'	0.40	1.20	2.00	2.80
C	-0.29	-0.52	-0.75	-0.98

when the echo fill fraction is above threshold. The local values of the summed reflectivity flags N, the summed clutter flags T, and the standard deviation flag S_R are used in the clutter decision-making model.

The threshold curves of the new decision-making model (see figure 3.2) are almost identical to those of the current clutter removal scheme, but the second-order polynomials that describe the threshold curves have been reformulated. The final clutter flag for the corresponding processed range bin is set when the clutter fraction T/N_s (on y-axis) for a certain echo-fill fraction N/N_s (on x-axis) is higher than the threshold curve. In the current clutter removal scheme the choice of the threshold curve depends on the value of the clutter flag of the twin bin ($T_{R2} = 0, 1, 2$). In the new scheme, the clutter flags T_R of the two neighboring range bins (see figure 3.1) are added to obtain a triple clutter flag $T_{R3} = 0, 1, 2, 3$ for the central range bin. Depending on the value of this triple flag and the standard deviation flag S_R the appropriate threshold curve is selected. The reformulated threshold polynomial of the clutter decision-making model is now given by :

$$\left(\frac{T_t}{N_s}\right) \equiv A \cdot \left(\frac{N}{N_s}\right)^2 + \left(B + \frac{B' \cdot R_0}{\max(R, R_0)}\right) \cdot \left(\frac{N}{N_s}\right) + C \qquad (3.16)$$

where T_t is the clutter flag threshold for the summed clutter flags T and R_0 is the minimum range. The values for the constants A, B, B' and C are listed in table 3.3 for the different values of the triple flag T_{R3} and the standard deviation flag S_R. If T is larger than T_t and the corresponding reflectivity flag is set, the final clutter flag for the central range bin is also set. In appendix A a part of the C source code for the processing of the clutter flags is listed.

a)

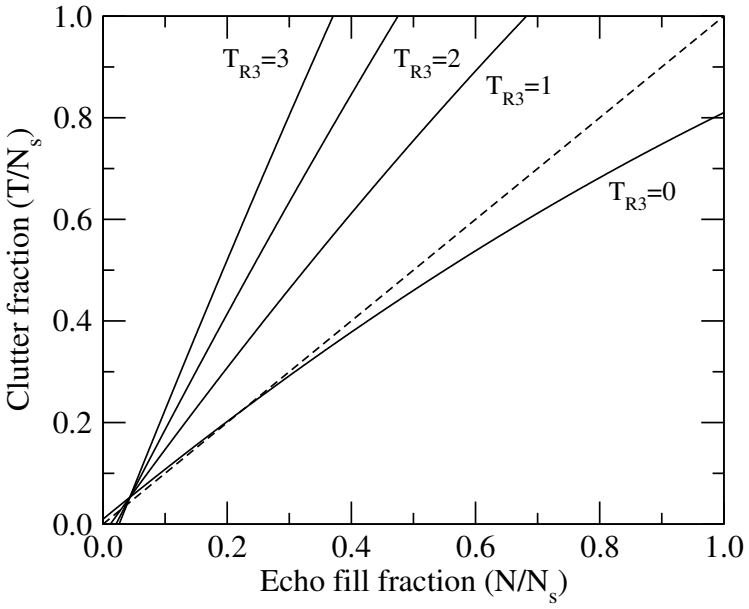

b)

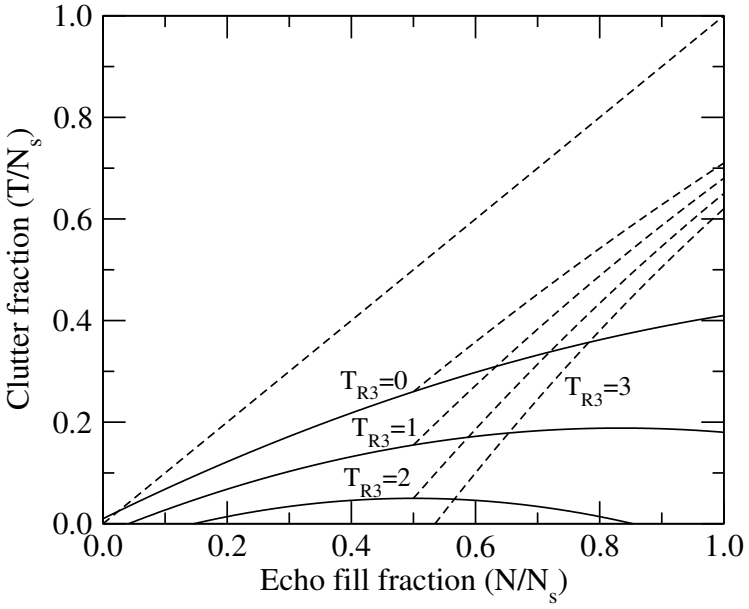

Figure 3.2: The threshold curves of the updated clutter decision making model are displayed in this figure. The upper frame **a)** shows the threshold curves for short ranges from the radar, and the lower frame **b)** shows them for long ranges. Four different threshold curves, one for each possible value of the clutter flag of the central twin bin T_{R3}, are presented in both frames.

(Raw dBZ) (T_{R3})

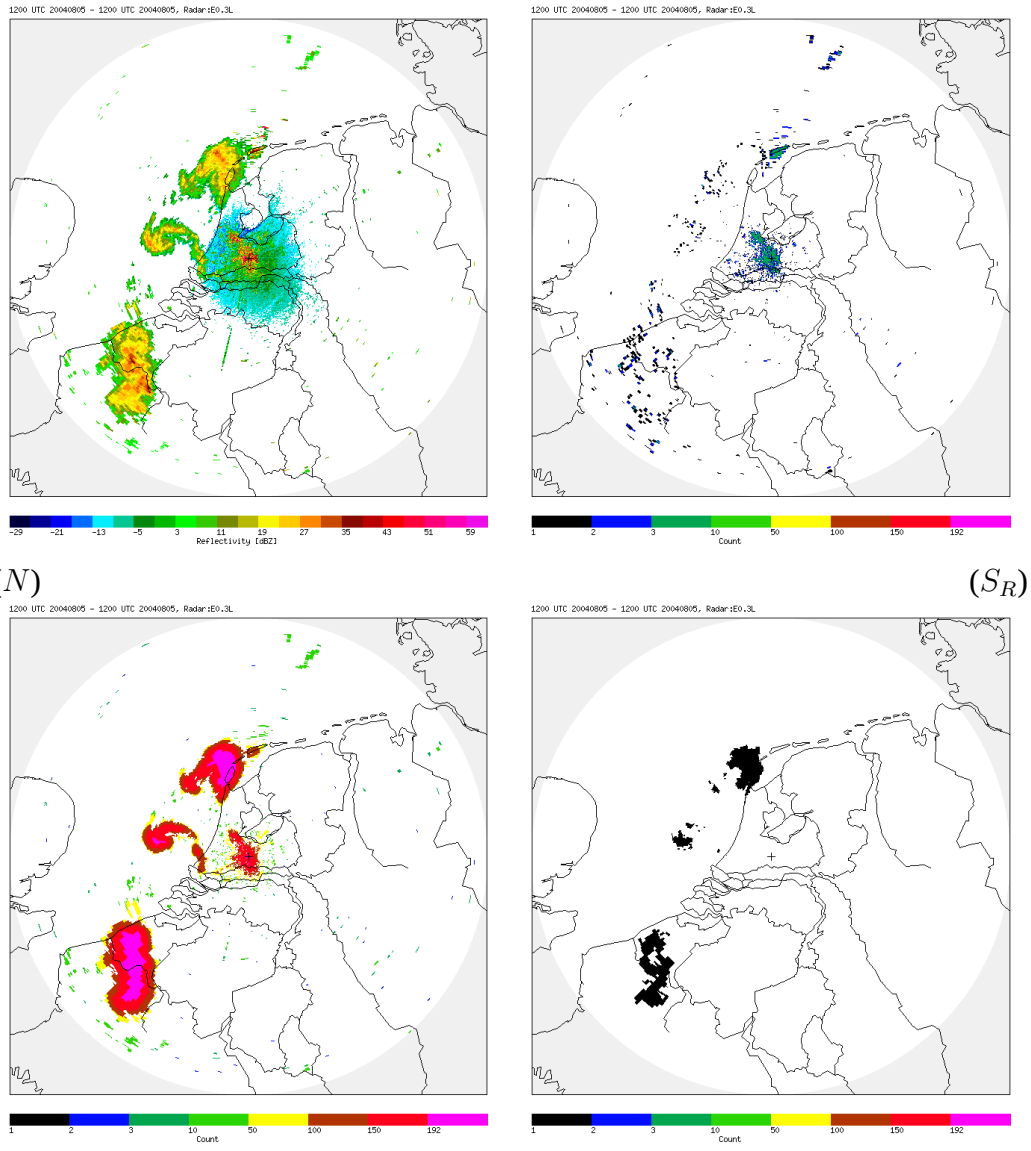

(N) (S_R)

Figure 3.3: Reflectivity and clutter flag data at the lowest elevation (0.3 deg) from the radar in De Bilt for 5 August 2004 at 1200 UTC. The raw reflectivity (upper-left), the triple clutter flag (upper-right), the summed reflectivity flags N (lower-left), and the deduced standard deviation flag S_R (lower-right) are shown in the four panels.

(T_t) (T)

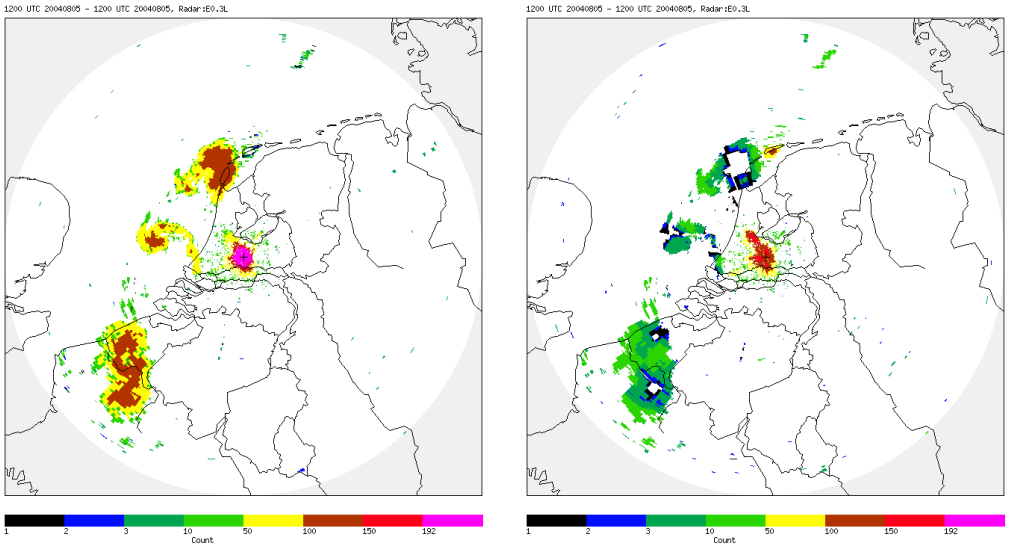

(Final clutter flags) (Clean dBZ)

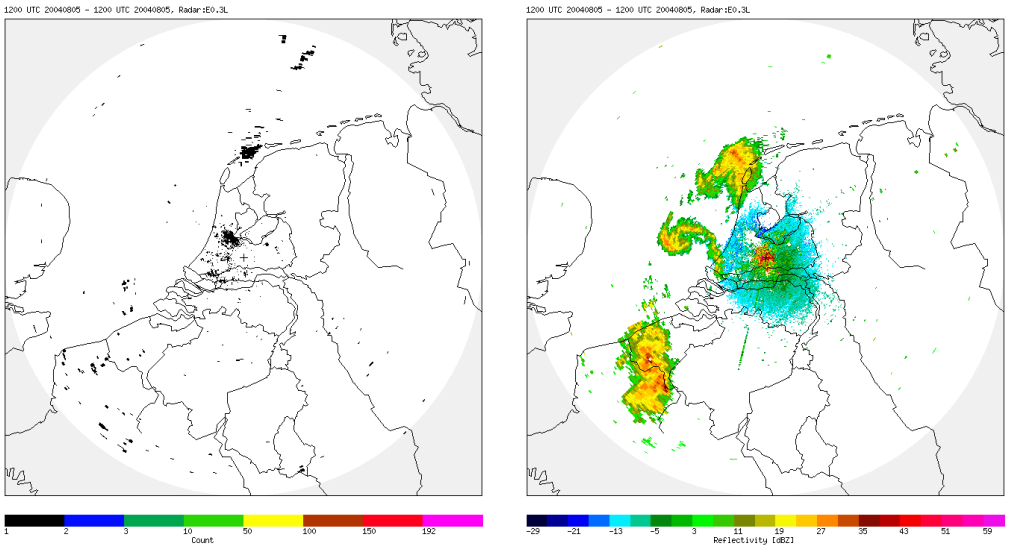

Figure 3.4: Idem as figure 3.3. The calculated clutter threshold T_t (upper-left), the summed clutter flags T (upper-right), the final clutter flags (lower-left), and the clean reflectivity (lower-right) are shown in the four panels.

The spatial averaging procedure of the new clutter removal scheme is illustrated using an example in figures 3.3 and 3.4. Data from the lowest elevation (0.3 degrees) from the radar in De Bilt are shown for 5 August 2004 at 1200 UTC. The polar data are shown in radar projection (azimuthal equi-distance) at a horizontal resolution of 1 km and the radar is in the center of the images. The upper-left and upper-right frames of figure 3.3 show the uncorrected reflectivity data and the triple clutter flags, respectively. In the reflectivity image, the sidelobe clutter around the radar and three precipitating systems south-west, west, and north-west of the radar can easily be distinguished. A closer examination of the image reveals strong clutter above the city of Amsterdam and a strong signal from the third Wadden island (Terschelling). The triple clutter flags T_{R3} give a clear signal around the radar site, above Amsterdam, and for the Terschelling island. So based on these two images, the areas with precipitation and with clutter can readily be distinguished by eye.

The lower-left image of figure 3.3 displays the summed reflectivity flags from the lowest elevation for 5 August 2004 at 1200 UTC. The three precipitating systems can be recognized by the large areas with high reflectivity flag values. The purple color in the figure represents a flag value of 192 which is the maximum value N_s according to equation 2.10 and table 3.2. The radar site, the city of Amsterdam and the Terschelling island are also visible in the reflectivity flag image but the maximum value is not reached. The standard deviation flags obtained from equation 3.15 are shown in the lower-left image of figure 3.3. Large areas with active standard deviation flags are observed in the centers of the precipitating systems.

From the summed reflectivity flags, the triple clutter flags, and the standard deviation flags, the clutter flag threshold T_t can be calculated using equation 3.16. The result is shown in the upper-left image of figure 3.4. Relatively high clutter thresholds of roughly 140 are obtained for the precipitating areas while a low threshold of 20 is found for the Terschelling island. The range dependence of the decision-making model caused by the B' term can clearly be seen from the high thresholds around the radar site. The summed clutter flags T from the lowest elevation for 5 August 2004 at 1200 UTC are shown in the upper-right image of figure 3.4. High values for the summed clutter flags, i.e., clearly larger than the threshold values, are only seen above the city of Amsterdam and around the Terschelling island.

The final clutter flags deduced from the upper images of figure 3.4 are shown in the lower-left image and the largest areas with flags are above Amsterdam and Terschelling. Finally, the lower-right image of the figure displays the reflectivity image cleaned using the final clutter flags in polar coordinates, i.e., as a function of range and azimuth. This cleaned reflectivity image should be compared to the raw reflectivity image in figure 3.3. A comparison between the current clutter

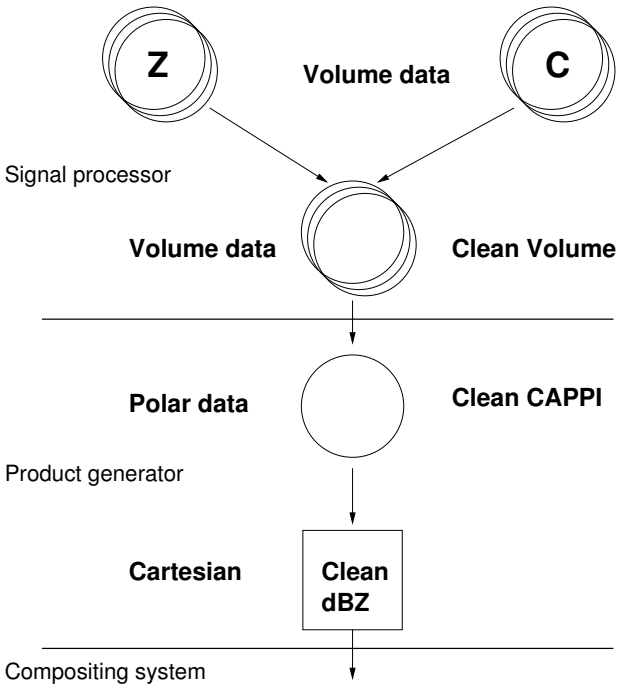

Figure 3.5: Flow diagram for the proposed implementation of the clutter rejection algorithm. On the left the systems where action is taken, i.e., the signal processor, the product generator, and the compositing system, are indicated

removal scheme and the proposed scheme is presented in chapter 4.

3.3 Clutter flag application

The application of the current clutter removal scheme is distributed over the signal processor (Sigmet, 1998), the product generator (Gematronik, 2003), and the compositing and distribution system (VCRIS). A flow diagram for the proposed implementation of the new clutter removal scheme is presented in figure 3.5. The new scheme can be handled completely by the radar signal processor and thus the implementation of the clutter removal scheme is simplified significantly. Before products can be generated from the clutter-corrected reflectivity data, an occultation correction has to be performed by replacing data for obstructed azimuths with interpolated data from neighboring azimuths. The cleaned reflectivity volume data can then be processed further using standard product generation software.

Chapter 4

Evaluation of the proposed scheme

In this chapter the results of an evaluation of the proposed clutter removal scheme is presented. The Cartesian data from the current operational clutter removal scheme are regarded as the reference data. For this study 3-dimensional volume data with the raw reflectivity and clutter flags from the signal processor have been collected. In this way the proposed clutter flag processing and clutter flag application were evaluated. The proposed changes in the clutter signal processing were not evaluated in this study because a digital IF signal processor was not available. Fortunately the proposed changes in the clutter signal processing are only minor and not likely to have a major effect on the performance of the removal scheme. The proposed changes in the clutter flag processing and application have been evaluated using three cases: a case with mixed precipitation and clutter, a case where the radome is wet, and a case of severe anomalous propagation. Furthermore a quantitative evaluation of the current and proposed clutter removal scheme using one month of (hourly) radar data is presented.

4.1 Case I: Mixed precipitation and clutter

The first case has been used already in section 3.2 to illustrate the decision-making process during the clutter flag processing. On 5 August 2004 the atmospheric flow above the Netherlands was rather weak and a thermally induced trough was aligned with the Dutch coast (see figure 4.1). The maximum temperature on this warm and dry summer day in De Bilt was about 30°C, the dewpoint temperature around 20°C, and the strength of the wind was 3 Beaufort. Three precipitating systems above the North Sea and strong clutter above the city of Amsterdam and above the Terschelling island are observed in the radar reflectivity data. This case of mixed precipitation and clutter was recorded by the radar in De Bilt around 1200 UTC. In the left column of figure 4.2 the clean pseudoCAPPI reflectivity

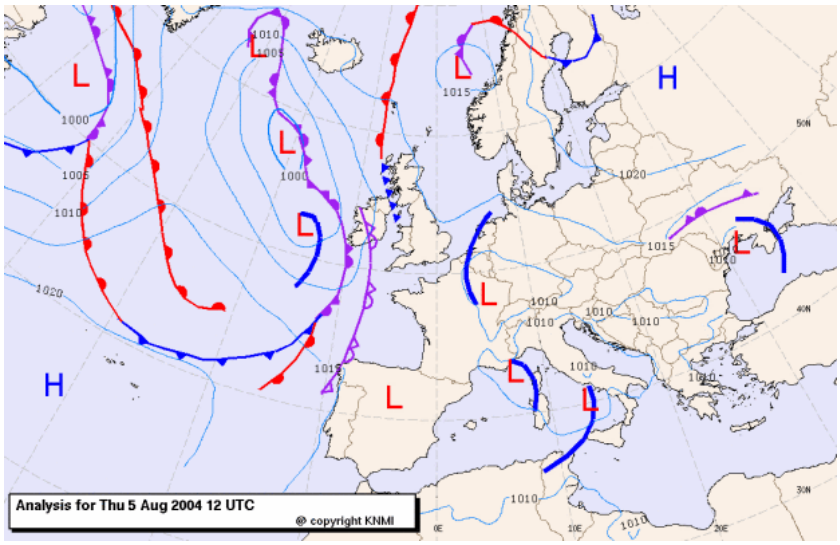

Figure 4.1: Analysis for 5 August 2004 at 1200 UTC based on the Hirlam numerical weather prediction model.

image and the corresponding clutter flag image obtained using the current clutter removal scheme are depicted. The reflectivity values have been converted to rain rates using the standard Z-R relation ($Z = 200R^{1.6}$) and the colors correspond to those of the KNMI radar display. Two colors have been added, however, at the low end (-15 dBR equal to 0.03 mm/h) and high end of the color scale (20 dBR equal to 100 mm/h). These two images have been generated from the operational data stream of the radar without any further processing.

The upper-right image of figure 4.2 shows the clean pseudoCAPPI reflectivity image obtained using the proposed clutter removal scheme described in chapter 3 and processed according to the flow diagram of figure 3.5. The generation of the pseudoCAPPI has been done according to the operational algorithm at KNMI which is based on an interpolation linear in dBZ instead of the usual interpolation linear in Z. To avoid unrealistic cut-offs at the edges of reflectivity patterns a so-called tophat value of -1.5 dBZ, where lower values are set to this tophat value, is applied. The geographical projection of the data from the azimuthal equi-distance projection ("radar projection") to the polar stereographic projection of the standard radar display of KNMI is done using the "proj.4" library (Evenden, 1990). Details on the geographical projection of the radar images are given in appendix B. It is evident from the two upper images of figure 4.2 that the clean reflectivity image obtained using the proposed clutter removal scheme is almost a photocopy of the current operational radar product. A closer examination of the

(Current clean dBZ) (New clean dBZ)

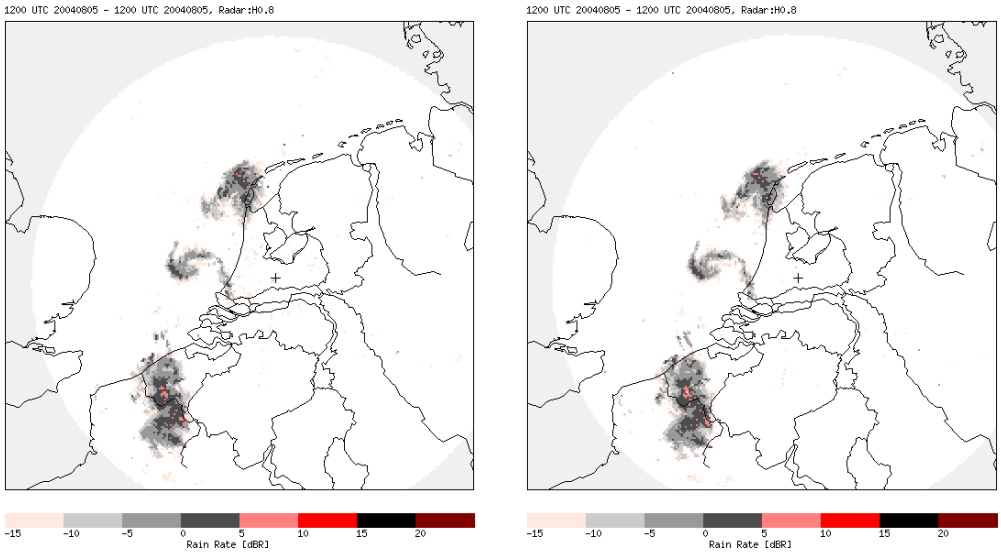

(Current clutter flags) (New clutter flags)

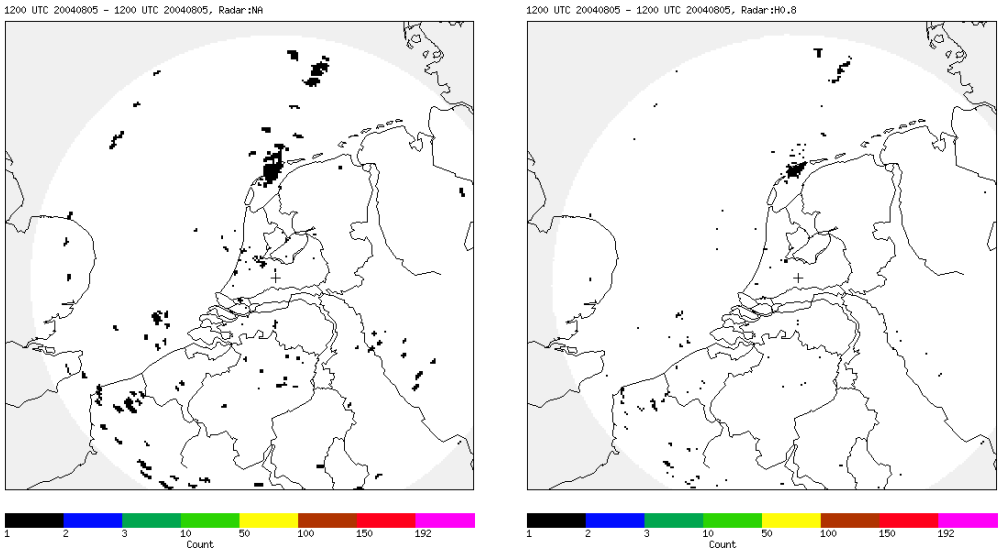

Figure 4.2: This figure shows pseudoCAPPI data (target height 800 meters) from the radar in De Bilt for 5 August 2004 at 1200 UTC. The clean reflectivity image (upper-left) and the clutter flag image (lower-left) using the currently operational clutter removal scheme are shown in the left column. The right column shows the clean reflectivity image (upper-right) and the clutter flag image (lower-right) for the proposed scheme.

images reveals, however, subtle differences at short ranges, where the proposed clutter removal scheme leaves less residual clutter.

For visualization purposes only, a Cartesian pseudoCAPPI clutter map has been generated using the proposed clutter removal scheme and it is shown in the lower-right image of figure 4.2. Note that this Cartesian clutter map is not used in the proposed clutter removal scheme because the clutter flags are applied on the 3-dimensional reflectivity data in polar coordinates (see figure 3.5). The pseudo-CAPPI clutter map at a target height of 800 meters is calculated by taking for each range the clutter flag from the elevation nearest to the target height. Comparing the clutter maps from the current and the proposed clutter removal scheme (two lower images of the figure), it appears the same features are present but the spatial extent of the features is larger for the current scheme. This comparison reveals an hidden feature of the current clutter removal scheme. Because of numerical inaccuracies in the conversion from polar to Cartesian and in the geographical reprojection, the spatial match between the cluttered reflectivity value and the corresponding clutter flag is sometimes lost. To fix this problem the clutter flag patterns in the Cartesian maps are artificially enlarged in the current scheme.

4.2 Case II: Wet radome

In the proposed clutter removal scheme the so-called wet radome correction (see section 2.2 for details) has been dropped. This wet radome correction is abandoned because its functionality largely overlaps with that of the range-dependent decision-making model. Clutter flags up to a certain range (25 km) are ignored due to the wet-radome correction for those azimuths where the echo at a predefined range (15 km) exceeds a predefined value (6 dBZ). The threshold curves of the decision-making model at short ranges (upper frame of figure 2.4) fall above (near) the $y = x$ line, so that the clutter flags will not (hardly ever) be set anyway. To illustrate that its justified to skip the wet-radome correction a case with intense rainfall in De Bilt has been selected. In figure 4.3 the observations of the automatic weather station in De Bilt are shown for 12 June 2005. Note that the horizontal axes in the graphs refer to local time which is two hours ahead of UTC. The third graph (from above) shows the rain rate in De Bilt as a function of time and at 1900 UTC an intense shower (roughly 12 mm/h) is observed.

The pseudoCAPPI data from the radar in De Bilt for 12 June 2005 at 1900 UTC is presented in figure 4.4. The left column of this figure shows the raw and clean reflectivity images obtained using the current operational clutter removal scheme. The strong resemblance of these reflectivity images indicates that there is hardly any clutter in the radar data at this moment. The reflectivity data shows a squall line just over the radar site (marked with a cross) which is

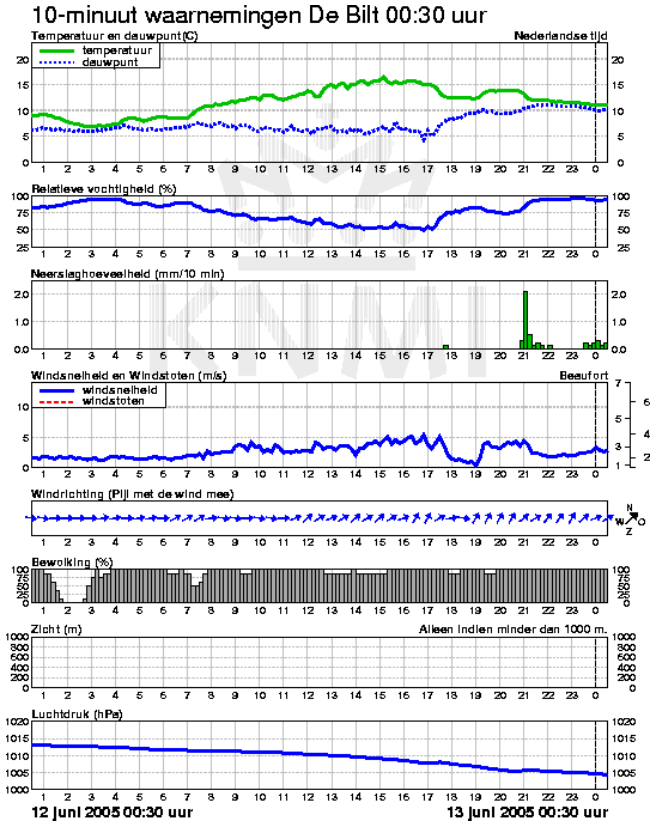

Figure 4.3: Observations of the automatic weather station in De Bilt at a 10-minute resolution for 12 June 2005 are shown. The horizontal axis represents the local time which is 2 hours ahead of UTC. The figure shows timeseries of the (dewpoint) temperature, relative humidity, wind direction and speed, rain rate, cloud cover, visibility, and surface pressure.

associated with a cold front. A few red pixels with $>$10 mm/h are observed close to the radar site which is in fair agreement with the 12 mm/h observed by the automatic weather station. This agreement is remarkable because a wet radome is known to produce strong attenuation of the radar radiation. The lower-right image of the figure displays the clean reflectivity data obtained using the proposed clutter removal scheme, i.e., without the wet-radome correction. It is evident from this reflectivity image that skipping the wet-radome correction does not do any (visible) harm. The clutter flag image (upper-right) obtained with the proposed scheme confirms that no flags are set around the radar site because of the rain.

(Current raw dBZ) (New clutter flags)

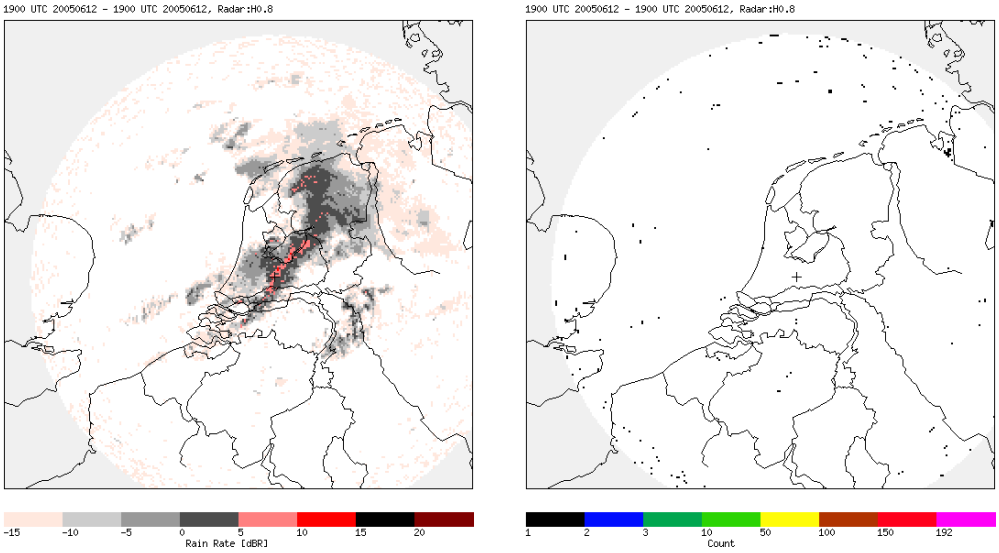

(Current clean dBZ) (New clean dBZ)

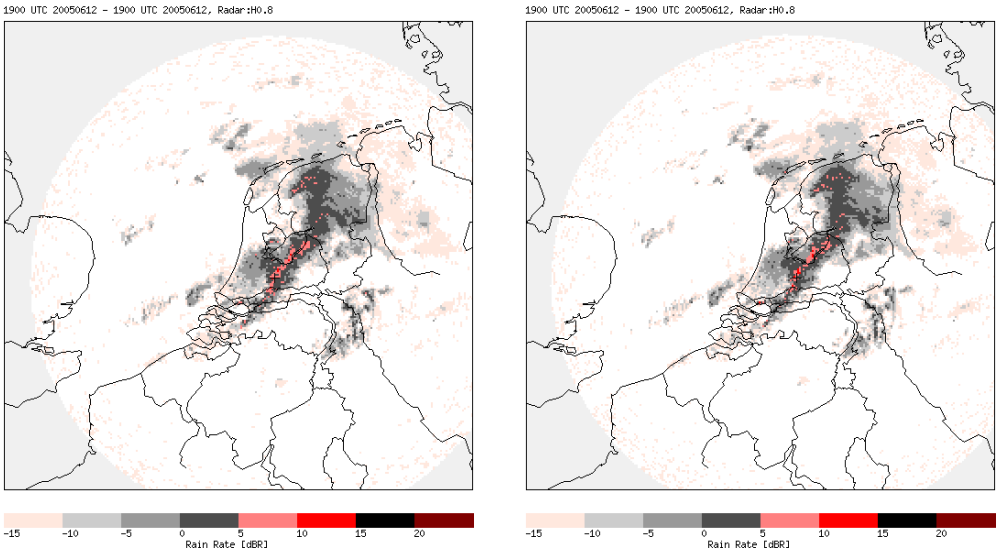

Figure 4.4: This figure shows pseudoCAPPI data (target height 800 meters) from the radar in De Bilt for 12 June 2005 at 1900 UTC. The raw reflectivity image (upper-left) and the clean reflectivity image (lower-left) using the currently operational clutter removal scheme are shown in the left column. The right column shows the clutter flag image (upper-right) and the clean reflectivity image (lower-right) for the proposed scheme.

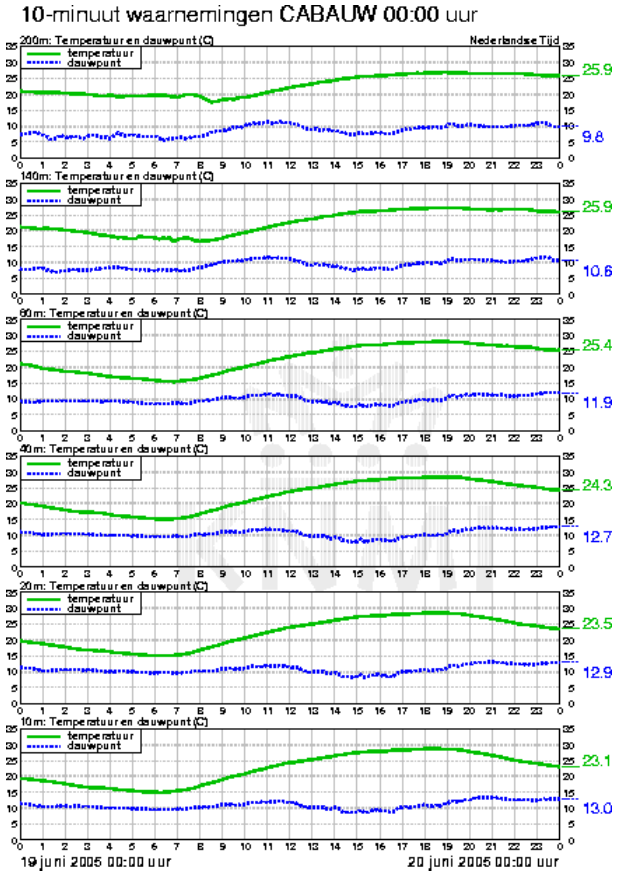

Figure 4.5: Temperature and dewpoint observations from the 213 meter tower in Cabauw at a 10-minute resolution for 19 June 2005 are shown. The horizontal axis represents the local time which is 2 hours ahead of UTC. The altitudes of the observations are 10, 20, 40, 80, 140, and 200 meters above ground level.

4.3 Case III: Severe anomalous propagation

Not much anomalous propagation clutter (anaprop) was seen in the first two cases and therefore a case of severe anaprop is discussed here. On 19 June 2005 a high pressure system resided over Denmark producing a (weak) flow from the south-east in the Netherlands. Maximum temperatures around 30°C were observed at many stations on this day. In figure 4.5 timeseries of the observed temperature and dewpoint from the meteorological tower in Cabauw (about 25 km south-west of De Bilt) on 19 June 2005 are shown. On this 213 meter tower observations are made at 6 altitudes between 10 and 200 meters above ground level. Note that the horizontal axes in the graphs refer to local time which is two hours ahead of UTC.

(Current raw dBZ) (New raw dBZ)

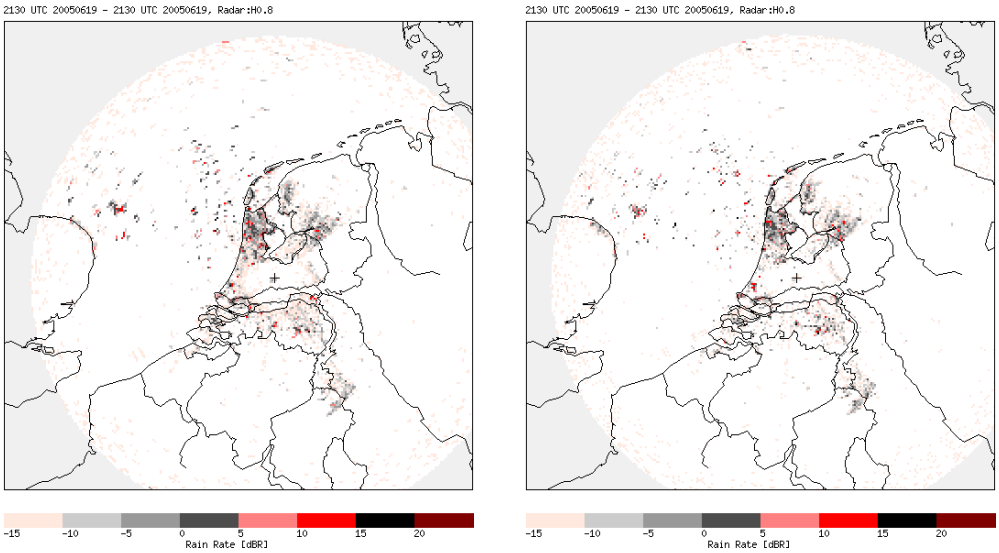

(Current clean dBZ) (New clean dBZ)

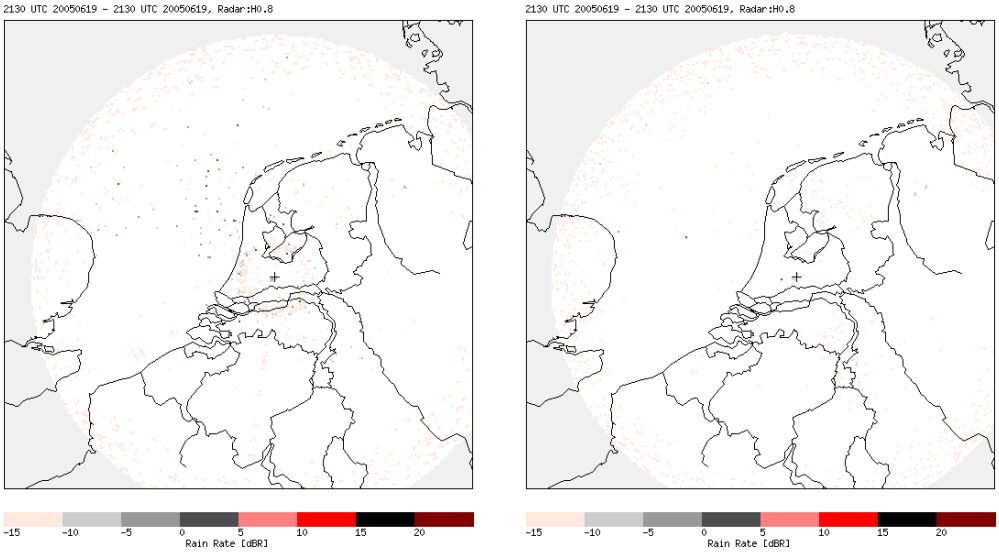

Figure 4.6: This figure shows pseudoCAPPI data (target height 800 meters) from the radar in De Bilt for 19 June 2005 at 2130 UTC. The raw reflectivity image (upper-left) and the clean reflectivity image (lower-left) using the currently operational clutter removal scheme are shown in the left column. The right column shows the raw reflectivity image (upper-right) and the clean reflectivity image (lower-right) for the proposed scheme.

A vertical temperature and dewpoint gradient of 14.7°C/km and -16.8°C/km, respectively, are observed between 10 and 200 meters in Cabauw around 2200 UTC. The refractivity N for radio-frequency radiation is related to the temperature T, the pressure p, and the partial pressure of water vapor p_w (Doviak and Zrnić, 1993):

$$N = \frac{77.6}{T}\left(p + 4810\frac{p_w}{T}\right) \tag{4.1}$$

where the pressures are given in mbar and the temperature in Kelvin. From this equation the refractivity gradient between 10 and 200 meters is determined as $dN/dh = -115$ km^{-1}. According to Doviak and Zrnić (1993) the typical refractivity gradient of the atmosphere in the first kilometer is -45 km^{-1} and thus the actual gradient on 19 June 2005 was much stronger than usual ("superrefraction").

In figure 4.6 the raw (upper row) and clean (lower row) reflectivity images obtained using the current clutter rejection scheme (left column) and the proposed scheme (right column) are shown for 19 June 2005 at 2130 UTC. There was no precipitation in the radar domain and thus all observed reflectivity is due to (anomalous propagation) clutter. The two raw reflectivity images should in principle be identical. The upper-right image has been produced from the reflectivity volume data using the off-line software developed for Research and Development work and the upper-left image is produced using the operational Rainbow software (Gematronik, 2003). The images are rather similar indeed, but a few remarkable differences can be seen. The (high) reflectivity cores, e.g. the sea clutter near the coast of the UK, are sometimes larger and less structured in the operational image. This difference can be attributed to the pairing of range bins into twin bins before projection to the Cartesian grid which has been not done in the off-line image. Another difference between the images is the position of the clutter at the coast of Norwich (UK) which is scattered around the coast line in the operational image and is accurately following the coast line in the off-line image. For the geographical projection of the operational image the Rainbow software uses the equations from Wessels (1990), and for the off-line image the radar projection is approximated by an azimuthal equi-distance projection and the proj.4 library (Evenden, 1990) is used for reprojection. In contrast to expectations it appears that latter procedure gives a (slightly) better result.

The clean reflectivity images obtained using the operational scheme and the proposed clutter rejection scheme are displayed in the lower row of figure 4.6. Most of the (sea) clutter is removed in both images. Note that the clutter removal scheme is only effective above 1 dBZ ($\simeq -13.8$ dBR) and thus the cluttered pink pixels are not removed completely. Clearly, the proposed clutter removal scheme produces a cleaner reflectivity image where the residual clutter close to the radar and especially the sea clutter are removed more effectively. The residual clutter close to the radar in the operational image is most likely caused by the applica-

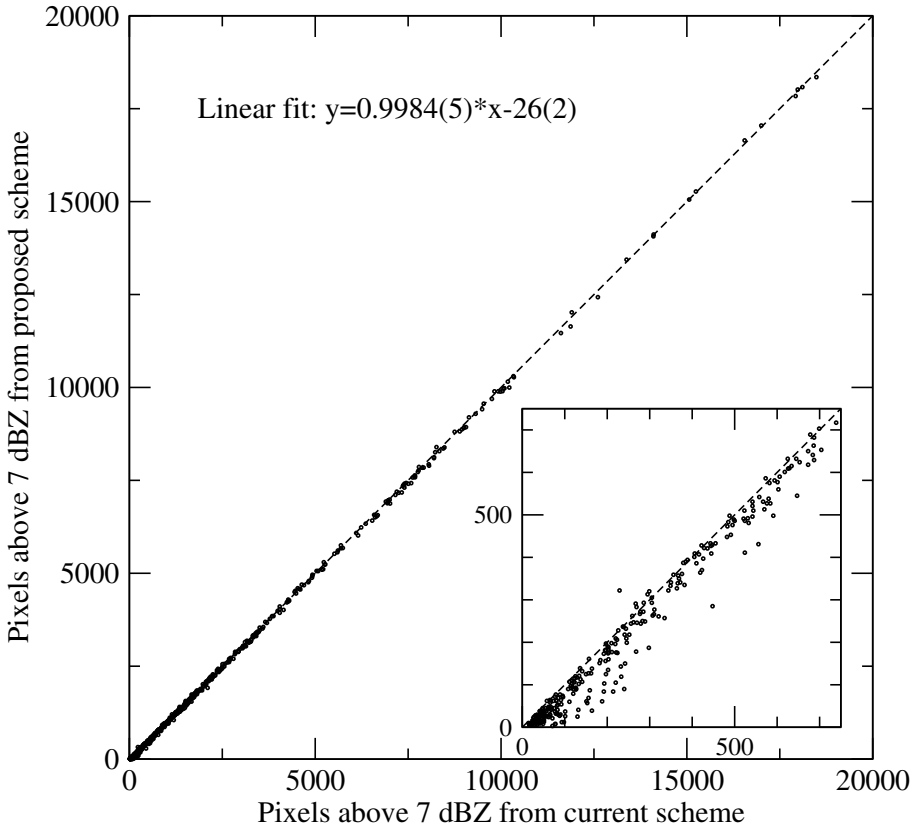

Figure 4.7: Scatter plot with the number of pixels with a reflectivity above 7 dBZ per image for the proposed clutter removal scheme and the current operational scheme. To ensure a certain degree of statistical independence the analysis is performed only once an hour at $hh00$ UTC. Radar data for May 2005 have been used for this scatter plot. The inset shows the scatter plot around zero.

tion of the clutter flags in the pseudoCAPPI image instead of per elevation. The remarkable additional reduction of sea clutter by the proposed scheme is probably due to the better spatial match between the cluttered reflectivity values and the corresponding clutter flags. Because of the application of the flags in the 3-dimensional reflectivity data in polar coordinates, numerical inaccuracies in the conversion from polar to Cartesian and in the geographical reprojection are circumvented.

4.4 Quantitative evaluation

In the previous sections the performance of the proposed clutter rejection scheme has been qualitatively evaluated using three cases. In this section a quantitative comparison between the proposed clutter rejection scheme and the current operational scheme using one month of radar data. From the raw reflectivity and clutter flag volume data clean pseudoCAPPI images with clean reflectivity data have been calculated. Volume data from the radar in De Bilt of May 2005 have been used. To ensure a certain degree of statistical independence only 3-dimensional volume scans recorded at $hh00$ UTC are processed. Furthermore the clean reflectivity images produced operationally at $hh00$ UTC by the radar in De Bilt have been collected over the same period. For all radar images the number of pixels containing a reflectivity stronger than 7 dBZ, i.e., the lowest level in the KNMI radar display, have been counted.

Figure 4.7 shows a scatter plot of the number of pixels above 7 dBZ for the clean reflectivity images obtained using the proposed clutter rejection scheme against that obtained using the operational scheme. It is evident that the numbers of 7 dBZ pixels from both rejection schemes are strongly correlated and are almost perfectly following the diagonal $y = x$. The number of 7 dBZ pixels in the analyzed images are scattered over a wide range from zero to almost 20,000. Note that the number of pixels in a KNMI radar image is 65,536 of which 51,689 are covered by the radar in De Bilt. In the "worst" cases (weak) precipitation is observed in almost 40% of the area covered by the radar (maximum range of 320 km). The inset of the figure shows in more detail the cases where hardly any precipitation is observed. It appears from this inset that the number of (residual) 7 dBZ pixels for dry cases is consistently larger for the operational rejection scheme. This observation is in accordance with the findings from the case of severe anomalous propagation (see section 4.3).

Using linear regression the relation between the number of 7 dBZ pixels obtained using the proposed scheme y and that using the current scheme x has been fit. The result is not shown in figure 4.7 because it cannot be distinguished from the dashed diagonal. The resulting line is given by:

$$y = 0.9984(5) \cdot x - 26(2) \tag{4.2}$$

where the number between brackets represents the statistical error in the last digit. The slope is very close to unity indicating that the proposed clutter rejection scheme removes hardly any additional precipitation pixels. The offset indicates that, independent of the actual precipitation, the proposed clutter scheme removes on average 26 additional pixels from each image. These are most likely the residual pixels that are more efficiently removed by the proposed clutter rejection scheme.

Chapter 5

Conclusions and recommendations

This review of the statistical clutter removal scheme, which is now operational at KNMI for more than 10 years, was initiated by the planned technical upgrade of the weather radars. The performance of the removal scheme is rather good and the customers of the radar products have hardly any complaints about residual clutter. Only residual sea clutter sometimes gives rise to dissatisfaction. The operational clutter removal scheme is effective on the 2-dimensional Cartesian radar products and its implementation is distributed over three different systems. A detailed description of the current operational clutter rejection scheme based on several reports and specification documents has been given in this report.

Currently the demand for the 3-dimensional volume data for research and operations is increasing. Therefore the review of the clutter removal scheme was focused on a transformation from a method for 2-dimensional Cartesian images to a method for 3-dimensional polar data. The most important advantages of such a transformation are:

- the production of clean 3-dimensional volume data that can be considered the base data from the weather radar systems in the (near) future.
- the implementation in the radar signal processor only and thus simplifying the radar processing chain.
- an improved performance of the clutter removal scheme because the pseudoCAPPI weighting and separate projection of clutter flags are circumvented.

In this report it has been documented in detail that the current clutter removal scheme can be transformed to a method for 3-dimensional polar data by a few minor modifications.

The performance of the proposed clutter rejection scheme has been evaluated using three cases: a case with mixed precipitation and clutter, a case where the

radome is wet, and a case of severe anomalous propagation. Furthermore a quantitative evaluation of the current and proposed clutter removal scheme using one month of (hourly) radar data is presented. It is found that the proposed scheme produces cleaner reflectivity images where the residual clutter close to the radar and the sea clutter are removed more effectively. Therefore it is highly recommended to implement the proposed clutter rejection scheme during the technical upgrade of the KNMI weather radars.

Acknowledgments

Herman Wessels is gratefully acknowledged for careful reading of the manuscript and for providing many useful comments.

References

Aoyagi, J.: 1983, A study on the MTI weather radar system for rejecting ground clutter. *Papers in Meteor. and Geophy.*, **33**, 187–243.

Doviak, R. J. and D. S. Zrnić: 1993, *Doppler Radar and Weather Observations*. Academic Press, second edition, 562 pp.

Evenden, G. I.: 1990, Cartographic Projection Procedures for the UNIX Environment — A Users's Manual. Technical report, United States Department of the Interior Geological Survey (USGS), www.remotesensing.org/proj/.

Gematronik: 1996a, Clutter Detection Specification. Gematronik GmbH., Raiffeneisenstr. 10, 41470 Neuss, Germany.

— 1996b, Clutter Post Processing Specification. Gematronik GmbH., Raiffeneisenstr. 10, 41470 Neuss, Germany.

— 2003, Rainbow 3.4 Operator's Manual. Gematronik GmbH., Raiffeneisenstr. 10, 41470 Neuss, Germany.

Kessinger, C., S. Ellis, J. Van Andel, J. Yee, and J. Hubbert: 2004, Current and Future Plans for the AP Clutter Mitigation Scheme. *20 Conference on Interactive Information and Processing Systems*, volume 12.5.

Parent du Châtelet, J., J. Testud, H. Andrieu, and P. Tabary: 2004, A first dual polarization weather radar in the French network: test of its usefullness for hydrology. *ERAD Publication Series*, volume 2, 421–424.

Siggia, A. D. and R. E. Passarelli Jr.: 2004, Gaussian model adaptive processing (GMAP) for improved ground clutter cancellation and moment calculation. *ERAD Publication Series*, volume 2, 67–73.

Sigmet: 1998, RVP6 Doppler Signal Processor User's Manual. Sigmet Inc., 2 Park Drive, Westford, MA 01886 USA.

Steiner, M. and J. A. Smith: 2002, Use of Three-Dimensional Reflectivity Structure for Automated Detection and Removal of Nonprecipitating Echoes in Radar Data. *J. Atmos. Ocean. Technol.*, **19**, 673–686.

Sugier, J., J. Parent du Châtelet, P. Roquain, and A. Smith: 2002, Detection and removal of clutter and anaprop in radar data using a statistical scheme based on echo fluctuation. *ERAD Publication Series*, volume 1, 17–24.

Wessels, H. R. A.: 1990, Coordinate conversions for presenting and compositing weather radar data. Technical report TR-129, Royal Netherlands Meteorological Institute (KNMI).

— 2003, Clutter Cancellation in KNMI Weather Radars. Chapter 4 of documentation.

Wessels, H. R. A. and J. H. Beekhuis: 1992, Automatic suppression of anomalous propagation clutter for noncoherent weather radars. Scientific report WR-92-06, Royal Netherlands Meteorological Institute (KNMI).

— 1994, Stepwise procedure for suppression of anomalous ground clutter. *COST-75 Seminar on Advanced Radar Systems*, EUR 16013 EN, 270–277.

Appendix A

Clutter flag processing

In this appendix a part of the C source code for processing of the clutter flags is listed. In this code it is assumed that the reflectivity in dBZ and clutter flags from the signal processing are provided for single elevation in arrays `zdata` and `cdata`, respectively. The data are stored ray-by-ray in the arrays. The final clutter flags and the cleaned reflectivity data are returned.

```
/*Constants for calculation of cluttermap:*/

#define CDBZMN (65+1)
#define SIGDBZ (7)
#define DAINN  (3)
#define DAOUT  (9)
#define DRINN  (7)
#define DROUT  (19)
#define DASTD  (5)
#define DRSTD  (11)
#define ETAMIN (0.5)
#define RNGMIN (7.0)

/*Clutter detection threshold polynomial: y=a*x*x+b*x+c, where x=N/Ns and */
/*y=Tr/Ns. The first index refers to S=0,1 and the second to T=0,1,2,3.*/

static float CLT_A[2][4]={{-0.2,-0.3,-0.4,-0.5},{-0.2,-0.3,-0.4,-0.5}};
static float CLT_B[2][4]={{0.6,0.5,0.4,0.3},{1.2,1.5,1.8,2.1}};
static float CLT_BR[2][4]={{0.4,1.2,2.0,2.8},{0.4,1.2,2.0,2.8}};
static float CLT_C[2][4]={{0.01,-0.02,-0.05,-0.08},{-0.29,-0.52,-0.75,-0.98}};

/*Calculation of summation limits.*/

dAinn=(DAINN-1)/2;
dAout=(DAOUT-1)/2;
dAstd=(DASTD-1)/2;
dRinn=(DRINN-1)/2;
dRout=(DROUT-1)/2;
dRstd=(DRSTD-1)/2;

/*Calculation of static sums.*/

Ns=(2*dAinn+1)*(2*dRinn+1)+(2*dAout+1)*(2*dRout+1);
```

```
S=(2*dAstd+1)*(2*dRstd+1);
Sxx=(dRstd*(2*dRstd*dRstd+3*dRstd+1)/6)*2*(2*dAstd+1);
Syy=(dAstd*(2*dAstd*dAstd+3*dAstd+1)/6)*2*(2*dRstd+1);

/*Setting reflectivity and clutter flags.*/

for (ia=0 ; ia<nazim ; ia++) {
   for (ir=0 ; ir<nrang ; ir++) {
      NRdbz[ir+ia*nrang]=TRclt[ir+ia*nrang]=0;
      if (zdata[ir+ia*nrang]>CDBZMN) {
         NRdbz[ir+ia*nrang]=1;
         if (cdata[ir+ia*nrang]) TRclt[ir+ia*nrang]=1;
      }
   }
}

/*Loop over all azimuths and ranges.*/

for (ia=0 ; ia<nazim ; ia++) {
   for (ir=0 ; ir<nrang ; ir++) {
      N=T=T3=Std2=S1=0;

/*Summation of reflectivity and clutter flags over Outer area.*/

      for (iia=ia-dAout ; iia<=ia+dAout ; iia++) {
         iaa=(iia+nazim)%nazim;
         for (iir=ir-dRout ; iir<=ir+dRout ; iir++) {
            irr=iir;
            if (irr<0) irr=0;
            if (irr>=nrang) irr=nrang-1;
            N+=NRdbz[irr+iaa*nrang];
            T+=TRclt[irr+iaa*nrang];
         }
      }

/*Summation of reflectivity and clutter flags over Inner area.*/

      for (iia=ia-dAinn ; iia<=ia+dAinn ; iia++) {
         iaa=(iia+nazim)%nazim;
         for (iir=ir-dRinn ; iir<=ir+dRinn ; iir++) {
            irr=iir;
            if (irr<0) irr=0;
            if (irr>=nrang) irr=nrang-1;
            N+=NRdbz[irr+iaa*nrang];
            T+=TRclt[irr+iaa*nrang];
         }
      }

/*Calculation of std dev of reflectivity and setting S=0-1 flag.*/

      if (N>Ns*ETAMIN) {
         Sz=Szz=Szx=Szy=0;
         for (iia=ia-dAstd ; iia<=ia+dAstd ; iia++) {
            iaa=(iia+nazim)%nazim;
            for (iir=ir-dRstd ; iir<=ir+dRstd ; iir++) {
               irr=iir;
               if (irr<0) irr=0;
               if (irr>=nrang) irr=nrang-1;
               Sz+=zdata[irr+iaa*nrang];
               Szz+=zdata[irr+iaa*nrang]*zdata[irr+iaa*nrang];
               Szx+=(iir-ir)*zdata[irr+iaa*nrang];
               Szy+=(iia-ia)*zdata[irr+iaa*nrang];
```

```
            }
         }
         Std2=(int)(Szz/S-Szx*Szx/(Sxx*S)-Szy*Szy/(Syy*S)-Sz*Sz/(S*S));
         if (Std2<SIGDBZ*SIGDBZ) S1=1;
      }

 /*Calculation of the TR3=0-3 index.*/

      if (TRclt[ir+ia*nrang]) T3++;
      if (ir>0&&TRclt[(ir-1)+ia*nrang]) T3++;
      if (ir+1<nrang&&TRclt[(ir+1)+ia*nrang]) T3++;

 /*Calculation of the threshold value.*/

      range=(ir+0.5);
      if (range<RNGMIN) range=RNGMIN;
      clt_b_sum=CLT_B[S1][T3]+CLT_BR[S1][T3]*RNGMIN/range;
      Tr=(CLT_A[S1][T3]*SQUARE((float)N/Ns)+clt_b_sum*(float)N/Ns+CLT_C[S1][T3])*Ns;
      if (Tr<0) Tr=0;
      if (Tr>Ns) Tr=Ns;

/*Setting the final clutter flag and cleaning of reflectivity data.*/

      if (T>Tr&&NRdbz[ir+ia*nrang]) flag=1;
      else flag=0;
      cdata[ir+ia*nrang]=flag;
      if (flag) zdata[ir+ia*nrang]=0;
   }
}
```

Appendix B

Geographical projection of KNMI radar images

In this appendix the details of the geographical projection of the KNMI radar images, both single site data and the national composite, are listed. The radar images are projected according to a stereographic projection with the northpole in the projection origin. A stereographic projection also uses a so-called alignment meridian (Greenwich) which is equal to the longitude of the projection origin and a latitude of true scale (60N). The stereographic projection is a conformal projection which implies that the angles are conserved during the projection. The meridians are projected into straight lines starting from the north pole and latitude circles are projected as circles centered at the north pole. It is important to stress that the KNMI radar images are projected using an ellipsoide earth model (Hayford). This makes the projection equations substantially more complex, but it enables a more accurate overlay of the radar echoes with the topographical data. The parameters of the geographical projection of the KNMI radar images are listed in the table below:

Parameter	Value
Projection	Stereographic
Projection origin (lon,lat)	0E, 90N
True scale (lat)	60N
Earth radius (equator,polar)	6378.388 km, 6356.912 km
Pixel size at true scale (x,y)	2.500 km, -2.500 km
Offset of image corner (i,j)	0.0, 1490.9
Number of rows	256
Number of columns	256

The geographical projection of the radar data from the azimuthal equi-distance projection ("radar projection") to the polar stereographic projection can be done

using the “proj.4” library (Evenden, 1990). This library has been developed at the USGS and is used world-wide in numerous applications. The geographical projection of the KNMI radar images is described by the following “proj.4 string”:

```
"+proj=stere +x_0=0 +y_0=0 +lat_0=90 +lon_0=0 +lat_ts=60 +a=6378.388 +b=6356.906"
```

After the geographical (re)projection the resulting image only has to be scaled and shifted linearly using the given pixel sizes and offsets of the image corner. The pixel size in y-direction is negative because the images lines are plotted from north-to-south and the y-axis is pointing in the opposite direction. The projection parameters define the geographical corners of the KNMI radar images. The corners of the KNMI radar image are:

Corner	Lon [deg]	Lat [deg])
north-west	0.000E	55.296N
north-east	9.743E	54.818N
south-east	8.337E	49.373N
south-west	0.000E	49.769N